BAMS Article

Measurements from inside a Thunderstorm Driven by Wildfire

The 2019 FIREX-AQ Field Experiment

David A. Peterson, Laura H. Thapa, Pablo E. Saide, Amber J. Soja, Emily M. Gargulinski, Edward J. Hyer, Bernadett Weinzierl, Maximilian Dollner, Manuel Schöberl, Philippe P. Papin, Shobha Kondragunta, Christopher P. Camacho, Charles Ichoku, Richard H. Moore, Johnathan W. Hair, James H. Crawford, Philip E. Dennison, Olga V. Kalashnikova, Christel E. Bennese, Thaopaul P. Bui, Joshua P. DiGangi, Glenn S. Diskin, Marta A. Fenn, Hannah S. Halliday, Jose L. Jimenez, John B. Nowak, Claire Robinson, Kevin Sanchez, Taylor J. Shingler, Lee Thornhill, Elizabeth B. Wiggins, Edward Winstead, and Chuanyu Xu

ABSTRACT: The 2019 Fire Influence on Regional to Global Environments and Air Quality (FIREX-AQ) field experiment obtained a diverse set of in situ and remotely sensed measurements before and during a pyrocumulonimbus (pyroCb) event over the Williams Flats fire in Washington State. This unique dataset confirms that pyroCb activity is an efficient vertical smoke transport pathway into the upper troposphere and lower stratosphere (UTLS). The magnitude of smoke plumes observed in the UTLS has increased significantly in recent years, following unprecedented wildfire and pyroCb activity observed worldwide. The FIREX-AQ pyroCb dataset is therefore extremely relevant to a broad community, providing the first measurements of fresh smoke exhaust in the upper troposphere, including from within active pyroCb cloud tops. High-resolution remote sensing reveals that three plume cores linked to localized fire fronts, burning primarily in dense forest fuels, contributed to four total pyroCb "pulses." Rapid changes in fire geometry and spatial extent dramatically influenced the magnitude, behavior, and duration of pyroCb activity. Cloud probe measurements and weather radar identify the presence of large ice particles within the pyroCb and hydrometers below cloud base, indicating precipitation development. The resulting feedbacks suggest that vertical smoke transport efficiency was reduced slightly when compared with intense pyroCb events reaching the lower stratosphere. Physical and optical aerosol property measurements in pyroCb exhaust are compared with previous assumptions. A large suite of aerosol and gas-phase chemistry measurements sets a foundation for future studies aimed at understanding the composition of smoke plumes lifted by pyroconvection into the UTLS and their role in the climate system.

KEYWORDS: Convection; Aerosols; Chemistry, atmospheric; Remote sensing; Field experiments; Wildfires

https://doi.org/10.1175/BAMS-D-21-0049.1
Corresponding author: David Peterson, david.peterson@nrlmry.navy.mil
Supplemental material: https://doi.org/10.1175/BAMS-D-21-0049.2

In final form 15 February 2022

AFFILIATIONS: Peterson, Hyer, and Camacho—Naval Research Laboratory, Monterey, California; **Thapa**—Department of Atmospheric and Oceanic Sciences, University of California, Los Angeles, Los Angeles, California; **Saide**—Department of Atmospheric and Oceanic Sciences, and Institute of the Environment and Sustainability, University of California, Los Angeles, Los Angeles, California; **Soja**—National Institute of Aerospace, and NASA Langley Research Center, Hampton, Virginia; **Gargulinski**—National Institute of Aerospace, Hampton, Virginia; **Weinzierl, Dollner, and Schöberl**—Aerosol Physics and Environmental Physics, Faculty of Physics, University of Vienna, Vienna, Austria; **Papin**—National Research Council, Monterey, California; **Kondragunta**—NOAA/Satellite Meteorology and Climatology Division, College Park, Maryland; **Ichoku**—College of Arts and Sciences, Howard University, Washington, D.C.; **Moore, Hair, Crawford, DiGangi, Diskin, Nowak, Robinson, Sanchez, Shingler, Thornhill, Wiggins, and Winstead**—NASA Langley Research Center, Hampton, Virginia; **Dennison**—University of Utah, Salt Lake City, Utah; **Kalashnikova**—Jet Propulsion Laboratory, California Institute of Technology, Pasadena, California; **Bennese**—San Jose State University, San Jose, California, and National Weather Service, Pendleton, Oregon; **Bui**—Earth Science Division, NASA Ames Research Center, Moffett Field, California; **Fenn**—Science Systems and Applications Inc., Hampton, Virginia; **Halliday**—Office of Research and Development, EPA, Durham, North Carolina; **Jimenez**—University of Colorado Boulder, Boulder, Colorado; **Xu**—I.M. Systems Group, College Park, Maryland

Fire-induced and smoke-infused thunderstorms, known as pyrocumulonimbus or pyroCb, are rapidly gaining scientific attention following the unprecedented wildfire activity observed in several regions worldwide since 2017. These unique storms act as "large chimneys" (Fromm et al. 2019), rapidly transporting smoke particles from the surface to the upper troposphere and lower stratosphere (UTLS). Smoke plumes injected into the lower stratosphere by recent pyroCb events in Canada and Australia have traveled around the globe, persisted for months, and altered dynamic circulation and radiative forcing across large regions (Peterson et al. 2018, 2021; Christian et al. 2019; Yu et al. 2019, 2021; Allen et al. 2020; Kablick et al. 2020; Khaykin et al. 2020; Torres et al. 2020; Das et al. 2021; Fromm et al. 2021; Lestrelin et al. 2021). This class of pyroCb smoke plumes rivals significant volcanic eruptions when comparing the aerosol particle mass injected into the stratosphere (Peterson et al. 2018, 2021). Motivation to understand the role of pyroCb activity in the climate system has therefore increased significantly, especially as seasonal fire activity continues to increase in severity in several fire-prone regions worldwide (Abatzoglou et al. 2019; Di Virgilio et al. 2019; Canadell et al. 2021). The 2019 Fire Influence on Regional to Global Environments and Air Quality (FIREX-AQ) experiment made a significant advancement in this endeavor by obtaining a diverse set of in situ and remotely sensed measurements of pyroCb activity over the Williams Flats fire in Washington State.

Existing measurements of pyroCb activity and ensuing smoke plumes in the UTLS are extremely rare. Since the advent of pyroCb research in the early 2000s (Fromm et al. 2000; Fromm and Servranckx 2003), only a few observational studies obtained in situ measurements with biomass burning characteristics in the UTLS that were attributed to a pyroCb source (Livesey et al. 2004; Dahlkötter et al. 2014). As understanding of pyroCb activity matured, mysterious smoke plumes identified in additional observational studies of the UTLS (Waibel et al. 1999; Jost et al. 2004; Ray et al. 2004; Reid et al. 2017) were eventually attributed to pyroCb activity (Fromm et al. 2019). However, all of these studies involved UTLS smoke plumes measured days to months after pyroCb cessation, well downwind of the fire.

Ground-based radar and lidar have been deployed in close proximity to fires, identifying the fine-scale dynamics of pyroCb activity and the pyrocumulus (pyroCu) precursor stage (Clements et al. 2018; McCarthy et al. 2018). When combined with radiosonde data, these observations provide detailed information on condensation within plumes and the influence of vertical wind shear (Lareau and Clements 2016). Recently, an airborne platform equipped with cloud radar and weather instrumentation provided observations of fine-scale plume dynamics involved in triggering pyroCb development as part of the Rapid Deployments to Wildfires Experiment (RaDFIRE; Clements et al. 2018). One flight transect penetrated a plume just below cloud base, revealing that pyroCb updraft speeds can rival those of supercell thunderstorms (Rodriguez et al. 2020). Radiation measurements within large pyroCu have also been obtained using an airborne platform (Gatebe et al. 2012). However, the few existing airborne measurements of pyroCu and pyroCb near the fire are limited to relatively low altitudes and do not include the high-altitude smoke outflow.

FIREX-AQ filled a significant observational gap by obtaining the first measurements from within the upper portion of an active pyroCb and young smoke outflow in the upper troposphere using the world's largest flying laboratory (NASA's DC-8 aircraft). Observations from the remote sensing payload on NASA's high-altitude ER-2 aircraft and ground-based weather radar provide additional information before and during pyroCb development. This diverse set of measurements serves as validation for a variety of existing studies that relied on satellite observations to characterize pyroCb activity (e.g., Fromm et al. 2005, 2008a,b, 2010, Rosenfeld et al. 2007). It provides the means to evaluate existing assumptions required to detect pyroCb activity from space (Peterson et al. 2017b) and model the ensuing UTLS smoke plumes in chemical transport and climate models (e.g., Christian et al. 2019; Yu et al. 2019). It also addresses several unknowns in pyroCb research, including the fire characteristics and fuel consumption contributing to pyroCb development and the effect of smoke on cloud particle microphysics. Information on aerosol optical properties and chemical transformations in the ensuing, high-altitude smoke outflow ultimately sets a foundation for future studies aimed at understanding the role of pyroCb activity in a warming climate.

Meteorology influencing pyroCb activity and airborne sampling

PyroCb activity sampled by FIREX-AQ at the Williams Flats fire began at approximately 2200 UTC [1500 local time (LT), UTC – 7 h] 8 August 2019 and persisted through 0400 UTC 9 August (2100 LT). During this period, the fire was located within a decaying high pressure ridge, directly ahead of a large low pressure trough approaching the Pacific Northwest coastline (Fig. 1a). This "ridge breakdown" synoptic weather pattern is well recognized for its role in supporting extreme fire behavior in several regions worldwide, including pyroCb development (Nimchuk 1983; Westphal and Toon 1991; Potter 2012; Peterson et al. 2015, 2017a, 2018, 2021). An approaching deep-layer trough facilitates moisture transport and decreased stability in the midtroposphere above a deep, hot, dry, and unstable near-surface mixed layer. This meteorological environment allows deep, moist convection to develop simultaneously with intense fire activity at the surface.

The 0000 UTC radiosonde sounding at Spokane, Washington (OTX), on 9 August (1700 LT 8 August) revealed an "inverted V" thermodynamic profile that fits a previously developed conceptual model for pyroCb development in western North America (Fig. 1b; Peterson et al. 2017a). A large dewpoint depression at the surface (high temperature and low dewpoint), combined with a nearly dry adiabatic lapse rate in the mixed layer, facilitated low fuel moisture, plume dominated fire behavior, and propensity for fire spotting (e.g., Sullivan and Matthews 2013; Egorova et al. 2020). The sounding also exhibited a deep moist layer in the midtroposphere, minimal stable layers to inhibit convection, and 1158 J kg^{-1} of convective available potential energy (CAPE) when lifting the most unstable parcel from the mixed layer.

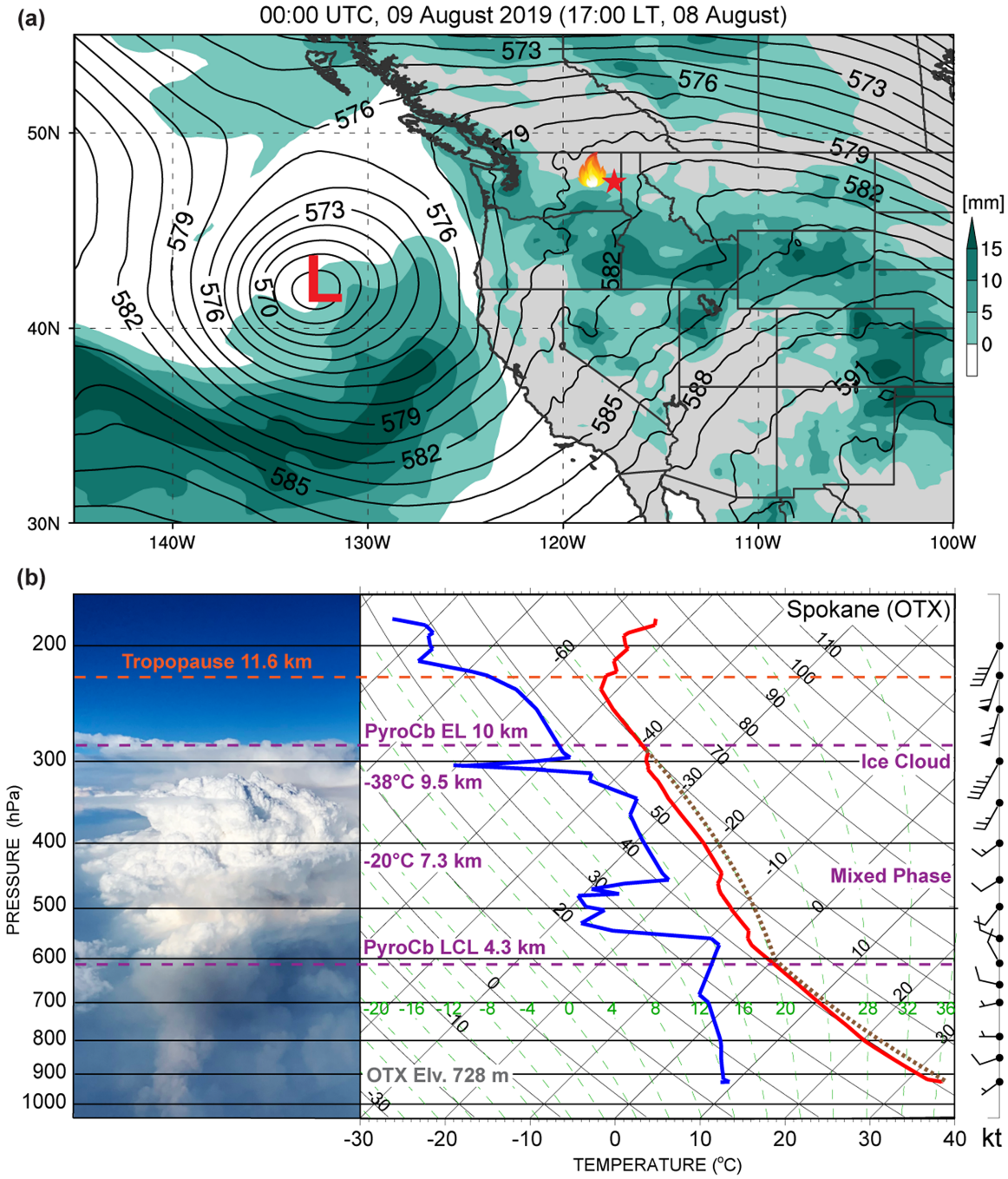

Fig. 1. Meteorology driving pyroCb activity over Williams Flats. (a) The map highlights the primary synoptic weather features during the pyroCb event (0000 UTC), with the center of an approaching trough denoted by a red "L." Black contours are 500-hPa heights from the ECMWF Reanalysis (ERA5). Green shading indicates positive anomalies of total column precipitable water derived from ERA5. The location of Williams Flats (47.98°N, 118.624°W) is marked with a fire symbol and Spokane, Washington (OTX), is identified with a red star. (b) A corresponding thermodynamic profile is provided from the OTX 0000 UTC radiosonde, with red and blue curves indicating the environmental temperature and dewpoint, respectively. Brown curve indicates the approximate pyroCb parcel path. Profile of wind speed and direction is displayed on the right (1 kt ≈ 0.51 m s^{-1}). Important vertical levels in the pyroCb cloud layer are annotated in purple text and dashed lines. Tropopause is marked by a dashed orange line. Photo from 0119 UTC provides an approximate visual reference for smoke plume and cloud characteristics at each vertical level.

While large CAPE is generally favorable for thunderstorm development, air parcels heated by the Williams Flats fire contributed additional instability, known as fire-induced CAPE (Potter 2005; Tory et al. 2018). This thermodynamic environment, combined with a relatively

low average wind speed in the mixed layer (5 kt or 2.6 m s^{-1}; 1 kt ≈ 0.51 m s^{-1}) and minimal shear, facilitated significant vertical smoke plume growth. Relatively small fire heating was therefore required to support an updraft capable of reaching the level of free convection, condensing, and ultimately triggering pyroCb development (Tory and Kepert 2021; Leach and Gibson 2021). This is true even when lifting a parcel derived from the upper portion of the mixed layer to account for potential entrainment and dilution within the rising plume (Fig. 1b, brown curve). PyroCb cloud tops reached approximately 10 km, coinciding with a weak stable layer [equilibrium level (EL)] in the upper troposphere. PyroCb activity did not overshoot the tropopause (11.6 km). The pyroCb lifting condensation level (LCL) was approximately 4.3 km (3.6 km above ground level at OTX), which is typical of high-based thunderstorms and pyroCb activity in western North America (Peterson et al. 2015, 2017a). The photo in Fig. 1b provides an example of the deep smoke plume and high cloud bases associated with the pyroCb activity sampled by FIREX-AQ.

Fire intensity was approximated during the primary burning period of the Williams Flats fire using an hourly time series of fire radiative power (FRP, units of MW; Peterson et al. 2015, 2021) retrieved from Advanced Baseline Imager (ABI) on the Geostationary Operational Environmental Satellite observing western North America (GOES-West, currently *GOES-17*), as shown in Fig. 2. Fire spread was approximated using nightly fire perimeter maps from the U.S. Forest Service (USFS) National Infrared Operations (NIROPS), revealing a gradual increase as the high pressure ridge broke down during 6–8 August (Fig. 1a). FRP concurrently increased during this period, especially during the local nighttime hours. Similar meteorology and deviations from a typical fire diurnal cycle were associated with the most extreme fire behavior and pyroCb activity observed during many previous events, including the 2013 Rim Fire in California (Peterson et al. 2015; Saide et al. 2015), the 2017 Pacific Northwest Event in Canada (Peterson et al. 2018; Fromm et al. 2021), and the 2019/20 Australian New Year Super Outbreak (ANYSO; Peterson et al. 2021). The FIREX-AQ forecasting team therefore recognized the potential for increasingly extreme fire behavior and moist pyroconvection (pyroCu and pyroCb) several days in advance. Small pyroCu were observed on 6 August and larger pyroCu were observed by the evening of 7 August. A separate pyroCb event preceded

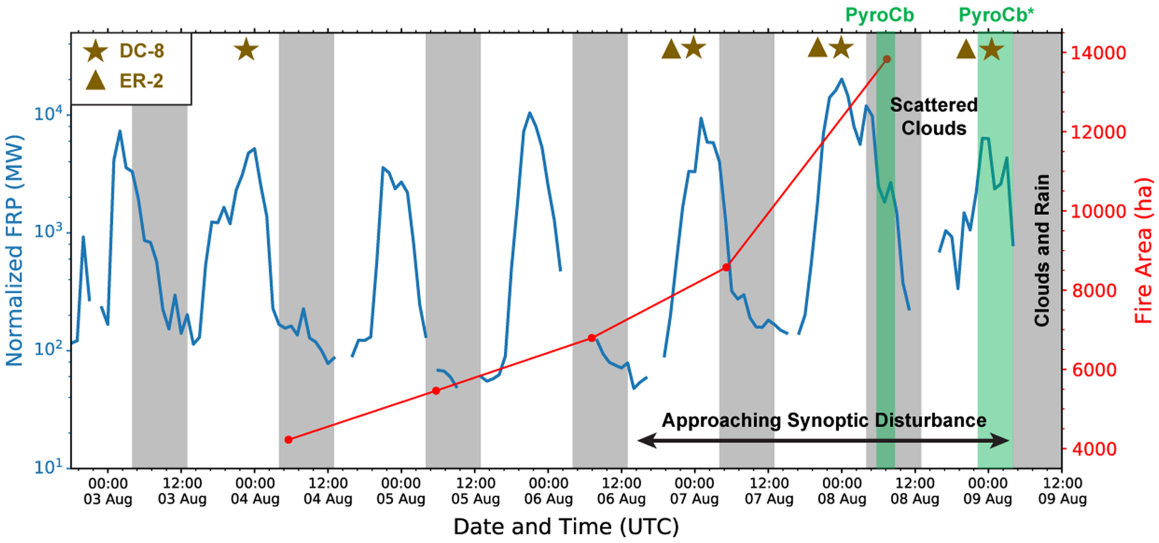

Fig. 2. Williams Flats time series of normalized hourly FRP from *GOES-17* (blue) based on the methods of Peterson et al. (2015, 2021) and cumulative fire area derived from nighttime NIROPS observations (red). PyroCb events are highlighted in green, with additional annotations provided for context and clarity. Nighttime periods are shaded in gray. Daytime periods coinciding with measurements from the NASA DC-8 and ER-2 aircraft are denoted by brown stars and triangles, respectively. The pyroCb event sampled by the DC-8 is marked by an asterisk, occurring during 2200–0400 UTC (1500–2100 LT) 8–9 Aug 2019.

the event sampled by FIREX-AQ, during the local nighttime hours of 7–8 August. A variety of measurements were obtained from instrumentation on the ground, mobile laboratories, and airborne platforms on all three days of this unique sampling phase, which culminated in direct pyroCb measurements on 8–9 August. The Williams Flats fire produced the only significant pyroCb activity observed in the western continental United States during the relatively inactive fire season of 2019. It was effectively extinguished by cooler conditions, rainfall, and even flash flooding in the days following the pyroCb activity. All measurements at Williams Flats were comprised of locally emitted smoke, with no mixing of smoke from other fires in the region.

PyroCb measurement strategy

The Williams Flats fire was sampled in detail by multiple FIREX-AQ platforms during 6–8 August 2019, including two aircraft (Fig. 2). NASA's ER-2 (high-altitude science platform; Fig. 3a) passed over the Williams Flats fire at 1815 UTC (1115 LT) 8 August, approximately 6.5 h before the DC-8. The ER-2 carried a remote sensing payload, providing high-resolution imagery of the fire activity that set the stage for pyroCb development, along with thermodynamic profiles, aerosol profiles, and information on smoke plume chemistry (Table ES1 in the online supplemental material). Figure 3b provides an example true color composite of the region surrounding Williams Flats from the enhanced MODIS Airborne Simulator (eMAS; 50-m spatial resolution), revealing dense smoke covering the fire prior to the onset of deeper mixing later in the day. An infrared, false-color composite (Fig. 3c) highlights the underlying fire activity by applying a threshold of −0.30 to a normalized difference index calculation based on the 2.382- and 2.084-μm bands (Dennison and Roberts 2009). The cluster of fire pixels along the southern edge of the expansive fire perimeter coincided with the start of a

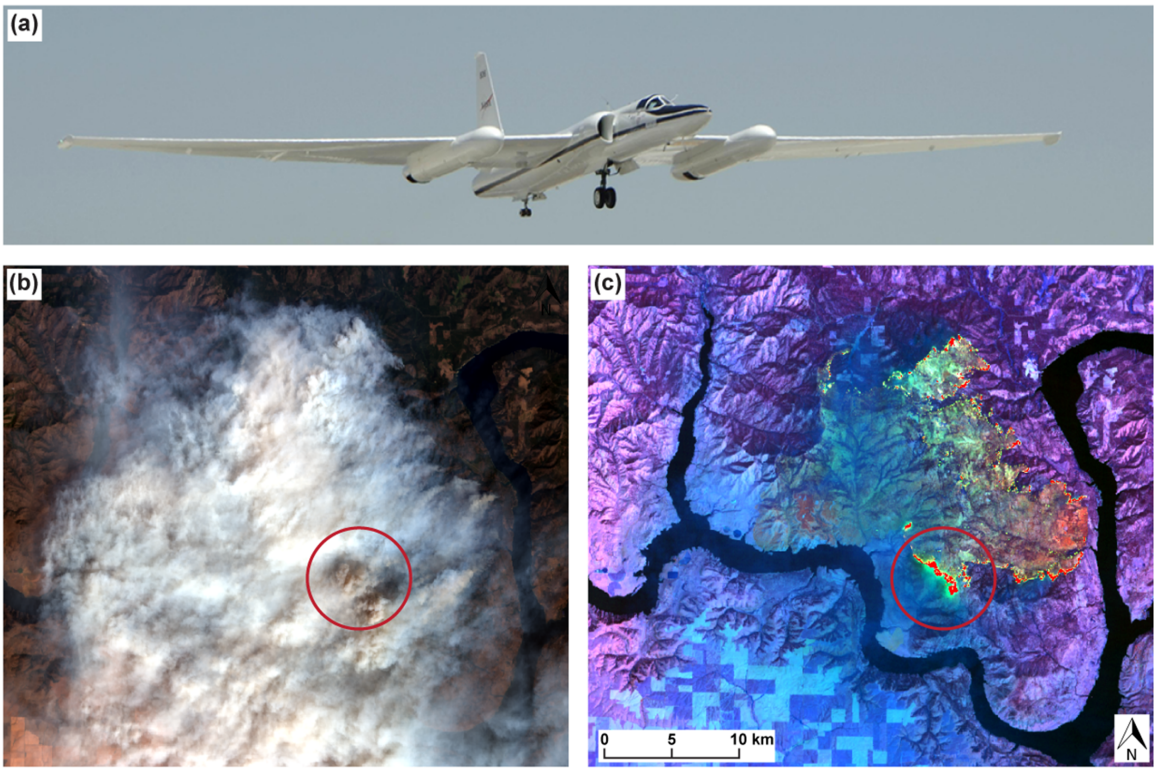

Fig. 3. Imagery from the Williams Flats ER-2 overpass at approximately 1815 UTC (1125 LT) 8 Aug 2019, including (a) photo of the NASA ER-2 high-altitude science platform, (b) true color composite from the enhanced MODIS Airborne Simulator (eMAS), and (c) infrared false color composite using the eMAS 8.515 μm (red), 2.382 μm (green), and 1.614 μm (blue) bands. Fire detections are shown in red using the methods described in Dennison and Roberts (2009).

localized fire spread event that ultimately set the stage for pyroCb development in this region later in the day.

All airborne measurements of the pyroCb activity and ensuing smoke plumes on 8 August were obtained from the NASA DC-8 (Fig. 4a). The DC-8 payload contained a comprehensive suite of aerosol and gas-phase chemistry instrumentation, with an emphasis on understanding chemical reactions and transformations in smoke plumes. The DC-8 also carried an up- and down-viewing lidar to obtain vertical smoke and cloud profiles and a multispectral imager for high-resolution mapping of fire characteristics. Two probes were included on the wings for sampling of aerosol and cloud microphysical properties. Ground-based weather radar [Spokane, Washington (KOTX), WSR-88D] provided additional perspective on the vertical profile of the pyroCb, cloud microphysics, and large ash particles lofted within the smoke plume. The combination of these airborne and ground-based observations provides the most comprehensive dataset currently available before and during an active pyroCb event.

PyroCb sampling focused on high-altitude smoke outflow between the altitudes of 6 and 10 km at a variety of distances from the fire. Figure 4b displays the entire pyroCb flight route, which spanned approximately 1.5 h. The DC-8 first intercepted the pyroCb smoke plume over northwestern Washington State near the Canadian border around 0050 UTC (1750 LT). The initial approach to Williams Flats generally progressed from older smoke outflow to the active pyroCb cloud tops over the fire. The middle portion of the flight focused on repeated plume transects immediately downwind of the active updraft core at multiple altitudes. The final portion of the flight generally progressed from the active pyroCb cloud tops back to older outflow downwind. Strong vertical motion and turbulence were avoided by remaining at relatively high altitudes, either above or downwind of the pyroCb updraft core.

The DC-8 provided 11 distinct sampling transects of this pyroCb event for in situ measurements between 0050 and 0215 UTC 9 August (8 August LT). Seven of these transects sampled within the pyroCb activity near the fire. Green lines in Fig. 4b highlight three longitudinal transects that sampled across the upper portion of the pyroCb, with smoke ages of a few minutes to an hour. Red lines highlight four cross-plume transects that sampled fresh outflow in the immediate anvil region (30–45 min old). Blue lines highlight four additional flight transects that sampled smoke aged over approximately 2 h in detached and decaying pyroCb anvil clouds, well downwind of the fire. Smoke age was determined as time since emission from the top of the pyroCb updraft core, derived from wind speed observations.

The time series of carbon monoxide (CO) in Fig. 4c represents an effective smoke tracer, highlighting the duration of each pyroCb plume transect along with aircraft altitude. Detailed mapping of the fire front with remote sensing instrumentation was conducted twice ("M" in Fig. 4c), focusing on regions that directly contributed to pyroCb development. Figure 4d provides a curtain plot from the Differential Absorption Lidar–High Spectral Resolution Lidar (DIAL-HSRL; Hair et al. 2008) on board the DC-8, highlighting the pyroCb exhaust as high backscatter values (mix of smoke and ice particles) at altitudes of 7–9 km, which are separated from lower-altitude smoke generally contained within the near-surface mixed layer below 4 km. This timeline provides a reference for specific sampling points and transects identified in subsequent figures, photos, and discussion.

Survey of DC-8 plume encounters

PyroCb activity over the Williams Flats fire occurred in four "pulses," defined as distinct, ice-capped convective columns from a single fire (Fromm et al. 2021; Peterson et al. 2021). In 1.5 h of sampling, the DC-8 obtained measurements from three of these pulses, including the active stage of pulses 2 and 3. Specific intervals sampling each pulse are provided in Fig. 4c and Table 1. The pyroCb pulses were generated by intense heat release associated

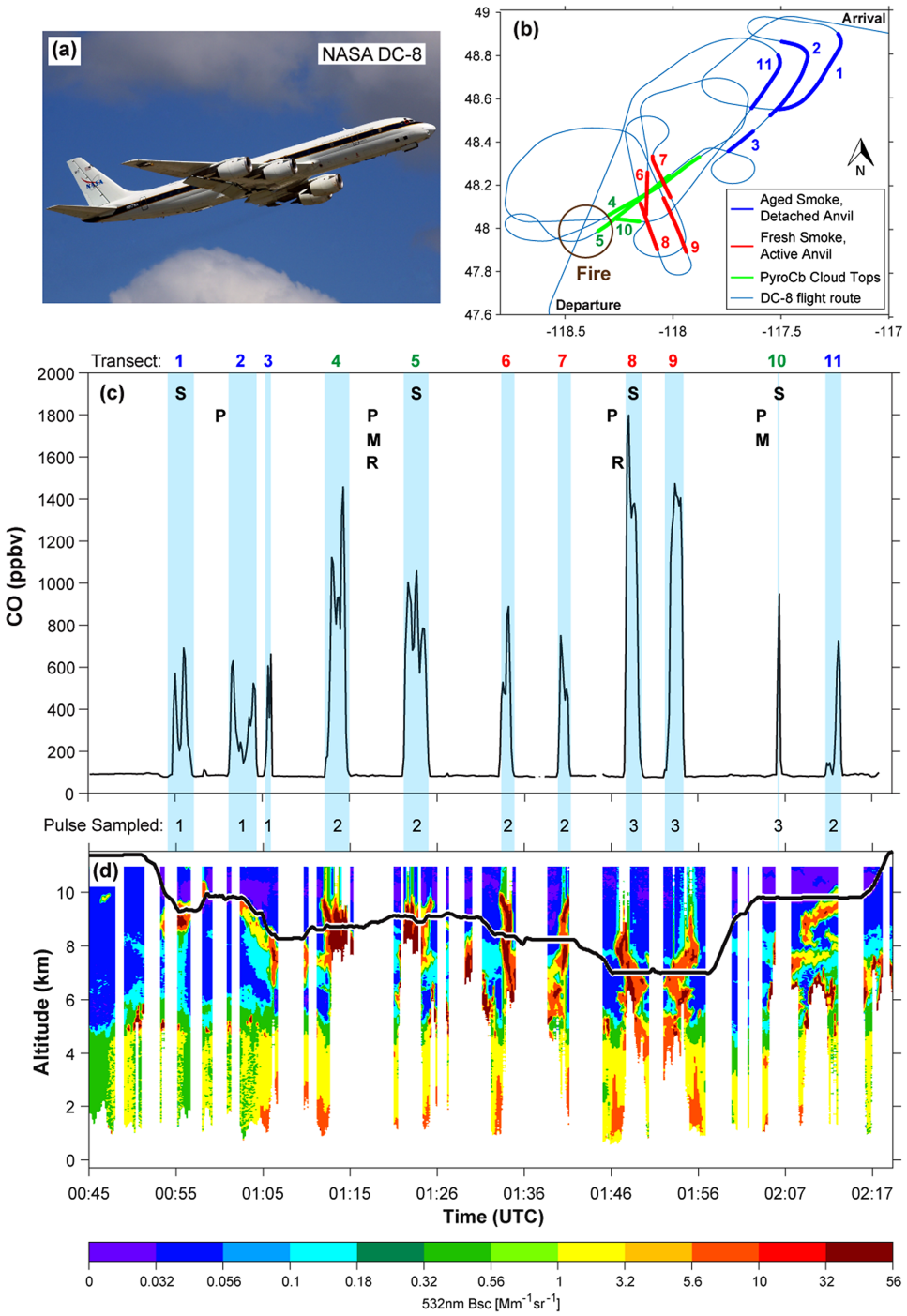

Fig. 4. PyroCb flight route and measurement timeline. (a) Photo shows the NASA DC-8 Flying Laboratory. (b) Map displays the entire pyroCb flight route on 9 Aug 2019 (8 Aug LT), with 11 in situ measurement transects color-coded based on smoke age and sampling technique. (c) The CO time series identifies the intervals of all 11 in situ transects, which are shaded in blue and numbered at the top. Letters coincide with the timing of content provided in subsequent figures, where "S" represents satellite imagery in Fig. 6, "P" represents photos in Figs. 5 and 7, "M" represents MASTER overpass maps in Fig. 8, and "R" represents radar volume cross sections in Fig. 10. Numbers at the bottom identify the pyroCb pulse measured in each transect. (d) The time series is atmospheric backscatter observed by the up- and down-viewing DIAL/HSRL lidar from the surface to the mean height of the tropopause (11.6 km). Large gaps indicate when the laser was turned off, primarily during steep turns. A few gaps at lower altitudes result from attenuation of the laser through the pyroCb cloud layer. Aircraft altitude is plotted as a black line.

Table 1. Details of four pyroCb pulses triggered by the Williams Flats fire.

PyroCb pulse (anvil cloud)	Time (UTC)[a]	Primary fire updraft region	Secondary fire updraft region
Pulse 1	2240–2330	1 (south)	—
Pulse 2	2330–0120	1 (south)	3 (north)
Pulse 3	0130–0300	3 (north)	2 (middle)
Pulse 4	0300–0400 after DC-8 flight	3 (north)	—

[a] All pyroCb activity in this table occurred during the local evening of 8 Aug 2019.

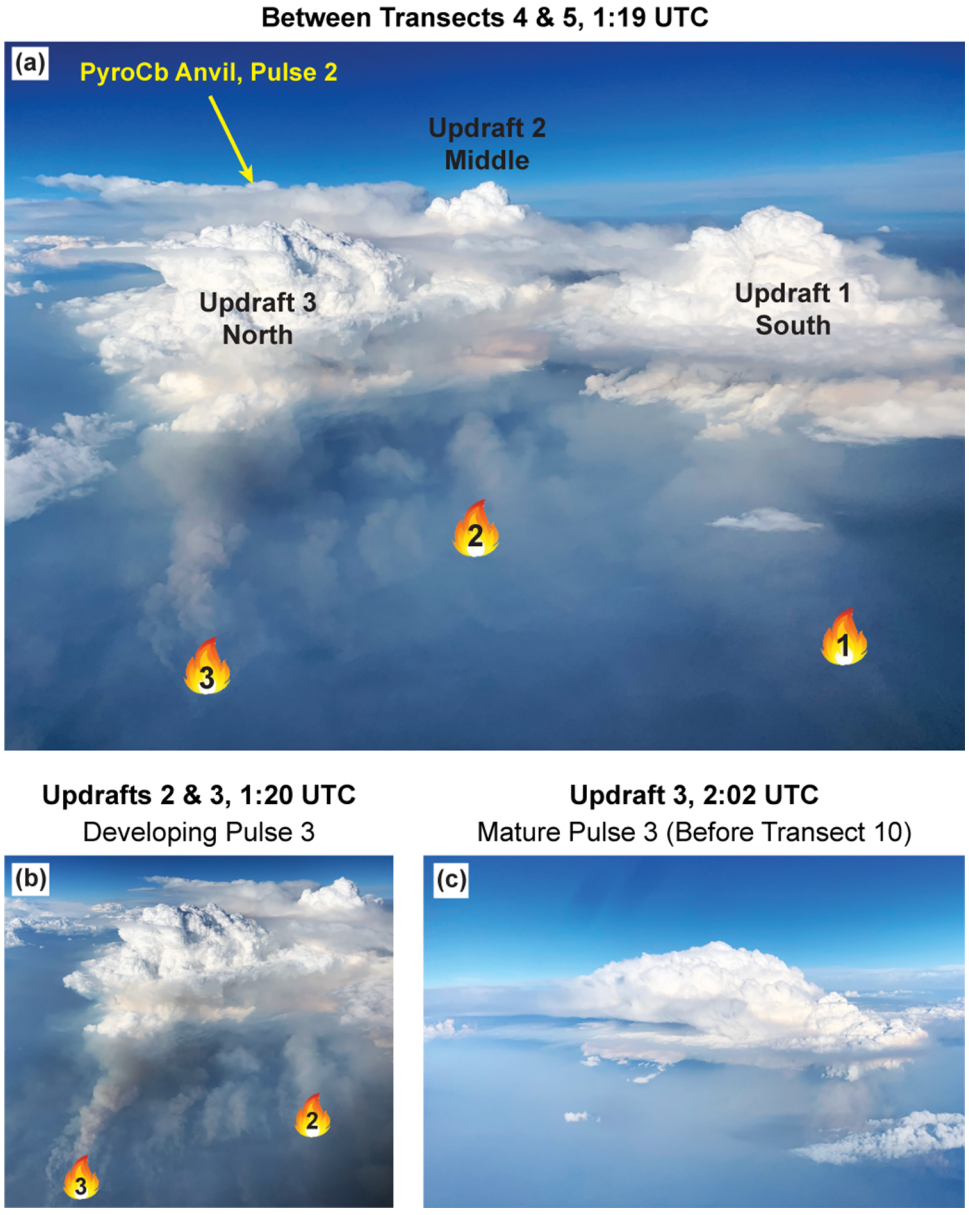

Fig. 5. Photos of significant pyroCb activity over the three Williams Flats fire updraft regions on 9 Aug 2019 (8 Aug LT), including (a) a complete view of the transition period between pulses 2 and 3 prior to the first MASTER overpass, (b) a close-up view of the developing third pulse (pyroCu stage, looking northeast) over the northern and middle portion of the fire front (updrafts 2 and 3), and (c) a complete view of the third pyroCb pulse at maturity (looking east from a distance) prior to the second MASTER overpass.

with three plume cores along distinct regions of the fire front (Fig. 5a). These visible regions are likely the areas of largest vertical velocity, and are therefore referred to as updraft regions.

The first pyroCb pulse (southern updraft region) reached peak intensity (highest injection altitude) at ~2240 UTC (1540 LT) 8 August, which is more than 2 h before the DC-8 arrived. The first three DC-8 flight transects (0054–0107 UTC) sampled the residual smoke-infused anvil cloud from this pulse (Fig. 4c), approximately 80–100 km downwind of the fire. A visualization of the first flight transect is provided in Fig. 6a, with the flight route superimposed on true color imagery from the *GOES-17* ABI. A photo around the time of this transect (0100 UTC) highlights the residual smoke layer at approximately 9.5 km as sublimation gradually dissipated the anvil ice cloud characteristics (Fig. 7a). This residual smoke layer at high altitudes represents the end result of the pyroCb process. In this case, the smoke layer was rapidly transported downwind following the jet stream winds in the upper troposphere. However, pyroCb activity can often overshoot the tropopause and inject smoke directly into the lower stratosphere (e.g., Fromm et al. 2008a,b, 2021; Peterson et al. 2018, 2021).

The second pyroCb pulse (southern and northern updraft regions) reached peak intensity while the DC-8 sampled the decaying anvil cloud from the first pulse (Fig. 6a, Table 1). The fourth and fifth transects made longitudinal passes directly through the upper portion of

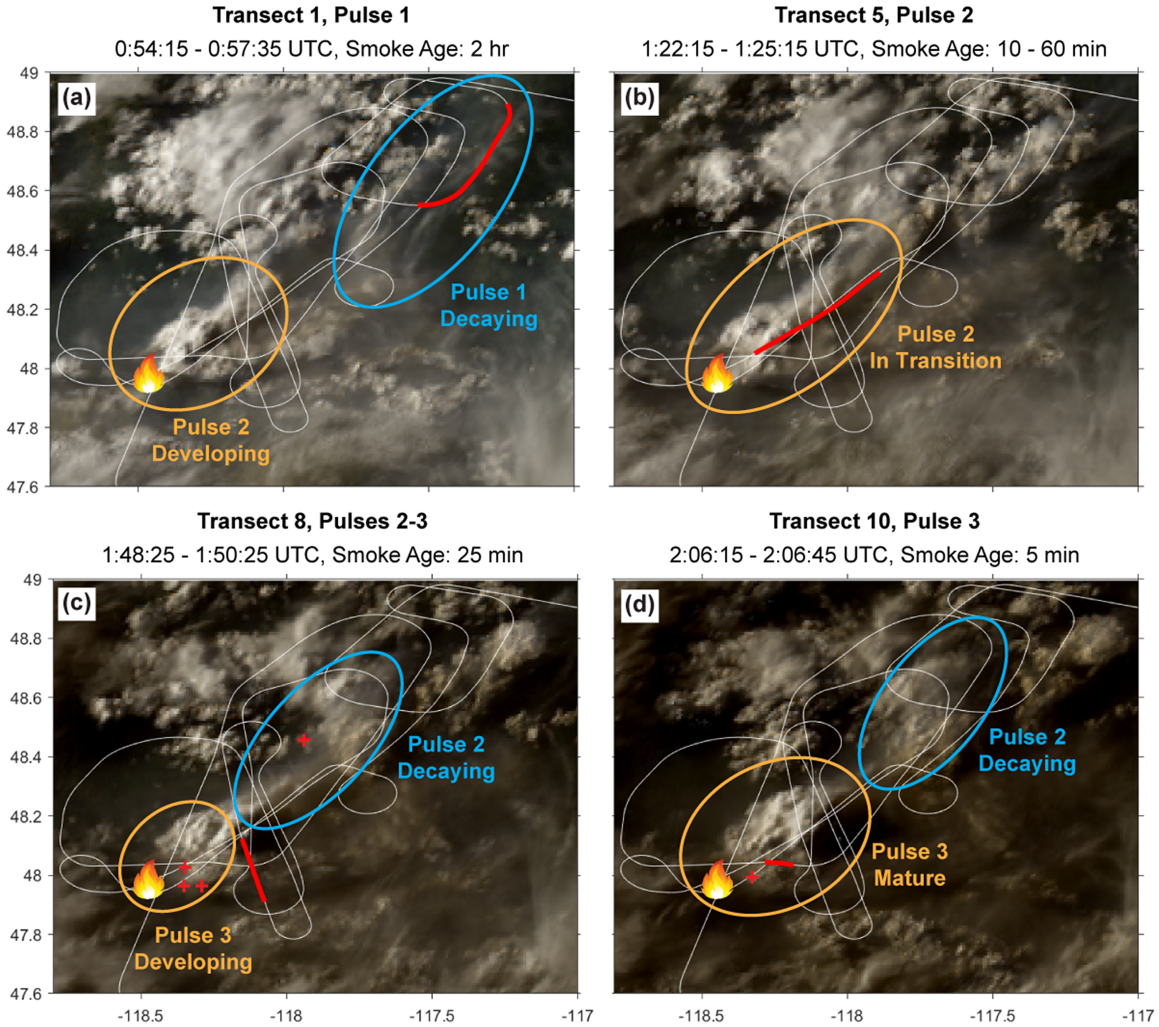

Fig. 6. ***GOES-17*** **true color imagery on 9 Aug 2019 (8 Aug LT) coincident with in situ measurement transects (red lines) in pyroCb (a),(b) pulses 1 and 2 and (c),(d) pulse 3. Developing, mature, and transitional phases are circled in orange, with detached, decaying pulses circled in blue. The Williams Flats fire is marked by a fire symbol. Red "+" symbols indicate Geostationary Lightning Mapper (GLM) lightning flashes observed within 10 min of each transect midpoint time. Images are not corrected for parallax.**

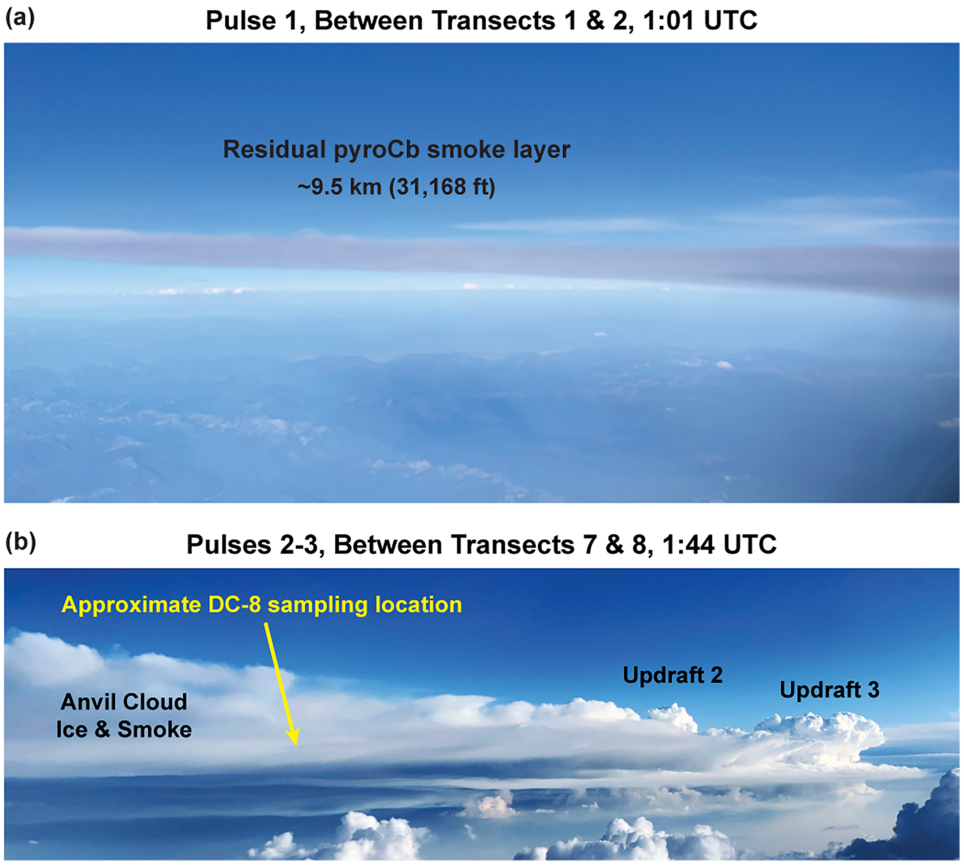

Fig. 7. Photos of strategic measurement periods in the high-altitude smoke exhaust downwind of the pyroCb updraft cores over the Williams Flats fire on 9 Aug 2019 (8 Aug LT), highlighting (a) residual smoke approximately 2 h after injection and (b) a smoky pyroCb anvil approximately 25 min after injection.

this pulse (Fig. 6b). A detailed view of the entire fire perimeter was captured from the cockpit during the turn between these transects, revealing the aforementioned three distinct updraft regions (Fig. 5a). This unique view coincides with a short transition period immediately after the second pulse detached from the fire and before the third pulse started to develop. While Fig. 5a shows large pyroCu over each updraft region, an active pyroCb pulse was not present immediately over the fire. Details of the fire characteristics contributing to pyroCb development are provided in the next section of this article.

To continue detailed measurements of fresh pyroCb outflow, the DC-8 began a series of transects perpendicular to the pyroCb anvil cloud layer slightly downwind of the updraft cores, with the first set (6 and 7) sampling above 8 km. Transects 8 and 9 repeated this sampling pattern, but at a lower altitude (7 km). The third and most intense pyroCb pulse rapidly developed during this period. Satellite imagery coincident with transect 8 (Fig. 6c) highlights the third pyroCb pulse over the fire and the decaying anvil of the second pulse moving downwind. This period also coincided with a significant shift in pyroCb activity from the southern updraft region to the northern and middle portion of the fire front (Fig. 5b, Table 1). While it is difficult to identify precisely when the DC-8 began sampling outflow exclusively from the third pulse, satellite and radar data suggest it likely occurred between transects 7 and 8 (Fig. 4c). A photo taken at this time (Fig. 7b) shows the large, smoke-filled pyroCb anvil and the approximate DC-8 sampling location, with the mature third pulse over the northern end of fire (updraft regions 2 and 3).

The final portion of the flight began with a second pass over the fire, focusing on the northern portion driving the active third pyroCb pulse. The DC-8 then conducted a final

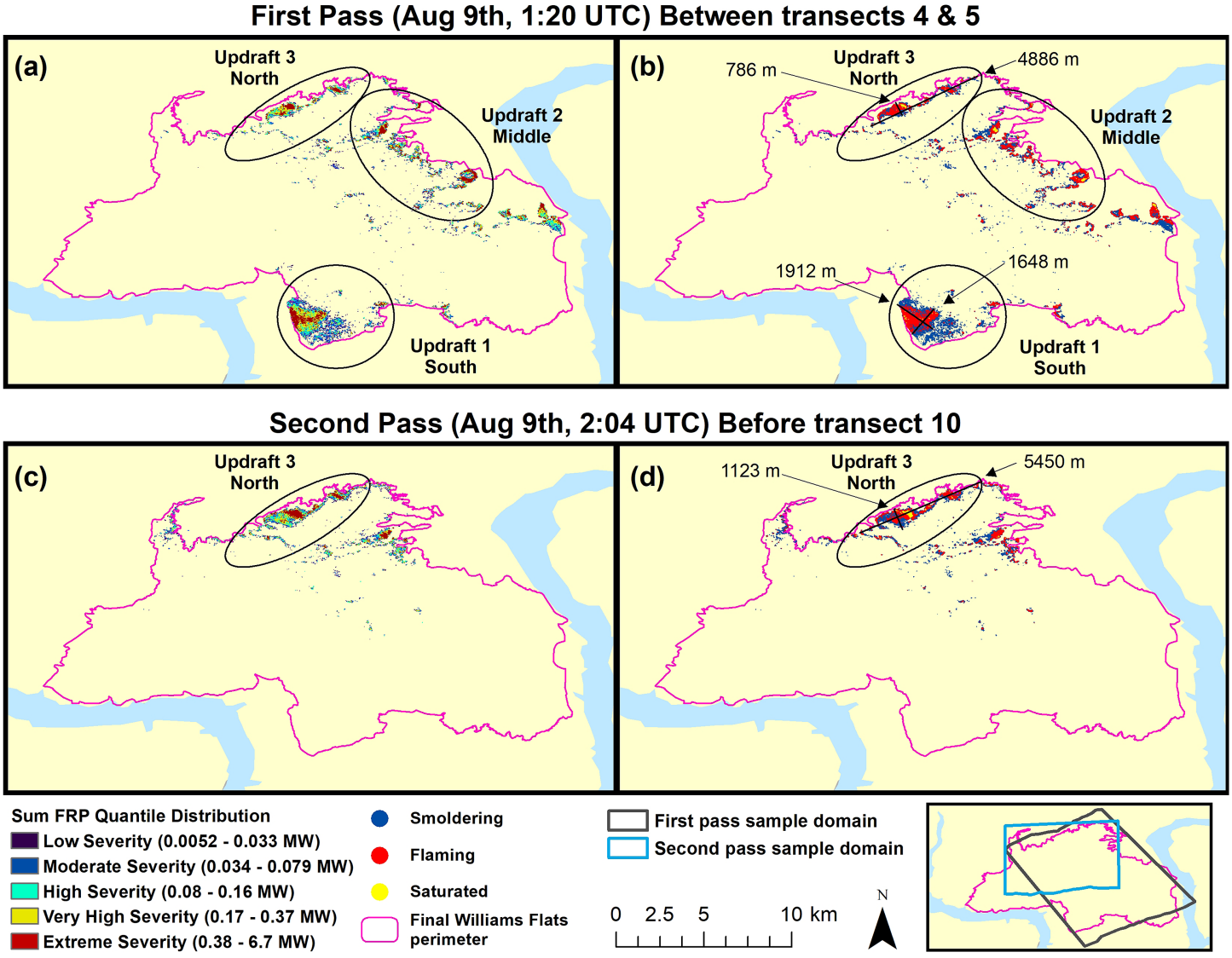

Fig. 8. (a)–(d) Characterization of MASTER fire radiative power (FRP) data for the Williams Flats fire on 9 Aug 2019 (8 Aug LT). Panels (a) and (b) coincide with the first MASTER overpass, and (c) and (d) coincide with the second overpass. The inset in the bottom right shows the sampling domain for each overpass. MASTER FRP data are equally distributed into quintiles in (a) and (c), representing the instantaneous energy released from the fire at the time of the overpass. MASTER-derived flags are shown in (b) and (d), representing smoldering, flaming, and saturated pixels. In all panels, updraft regions associated with pyroCb pulses are identified.

longitudinal transect (Fig. 6d) that passed directly through the upper portion of the third pulse (transect 10) and concluded by sampling the decaying anvil of the second pulse well downwind (transect 11). Figure 5c provides a photo taken as the DC-8 turned toward the fire to begin this portion of the flight, highlighting the mature third pulse at the northern edge of the fire. Lightning strikes precluded additional sampling of the pyroCb activity near the fire and the DC-8 returned to FIREX-AQ headquarters in Boise, Idaho. The final pyroCb pulse developed after the DC-8 departed (Table 1).

Quantitative fire characteristics

By 0120 UTC (1820 LT 8 August) Williams Flats burned primarily on three individual intense fire fronts within a larger parent fire perimeter (Figs. 5a and 8). These conditions created a complex sampling environment, because each updraft region contributed to at least one of the three pyroCb pulses sampled (Tables 1 and 2). The MODIS/ASTER Airborne Simulator (MASTER) obtained a snapshot of the entire fire front after the initial approach, as the second

pyroCb pulse began to decay, allowing the anvil to detach from the fire (0120 UTC; Figs. 8a,b). The southern updraft region likely reached peak fire intensity before the DC-8 arrived (first pulse), and was decreasing in intensity when sampled (0.2% saturated pixels). A second overpass 44 min later (0204 UTC) was limited to the northern portion of the fire (Figs. 8c,d), coinciding with the active phase of the third pyroCb pulse. FRP nearly doubled in the northern region during this timeframe, with 4% of the pixels saturated. These MASTER observations therefore provide a rare, high-resolution view of fire characteristics contributing to pyroCb development in real time, demonstrating the speed at which multiple pyroCb pulses can be generated, given the available fuels and ambient meteorology. The southern and northern updraft regions were not obscured by cloud cover due to a tilt of the smoke column and pyroCb activity downwind (Fig. 5).

MASTER provides the midinfrared (MIR) and thermal infrared (TIR) spectral channels (at approximately 4 and 11 μm, respectively) that are necessary to detect active fires using contextual algorithms and calculate FRP, as has become customary in satellite and airborne fire remote sensing (e.g., Giglio et al. 2003, 2016; Wooster et al. 2003, 2005; Peterson et al. 2013; Schroeder et al. 2010, 2014). For the pyroCb sampling period, irregularly spaced MASTER data were georeferenced in ArcGIS to an approximate 25–30-m pixel resolution, based on the variable DC-8 altitude (6–9 km) relative to the ground (E. Fraim 2021, personal communication). A 30-m grid was overlaid on the MASTER data, and FRP data were accumulated in each cell. Five fire-severity rankings were generated based on the quintiles of the resulting FRP distribution (Figs. 8a,c, Fig. ES1), which coincide with the five U.S. Forest Service (USFS) Wildland Fire Assessment System (WFAS) Fire Danger Class ratings (Deeming et al. 1977; Bradshaw et al. 1984).

Radiance saturation can occur for intense fires, with the impact varying by scene and aircraft altitude. The percentage of pixels affected by saturation ranged from 0.2% to 4.0% for all three fire updraft regions at Williams Flats, including both MASTER overpasses. While the saturation rates are relatively low in this analysis, saturated pixels can represent a large fraction of the most intensely burning pixels, and the impact on FRP totals for individual fire scenes can be significant (Schroeder et al. 2014). MASTER FRP data therefore underestimate the true total FRP for Williams Flats to varying degrees. Each nonsaturated MASTER pixel was classified as predominantly flaming combustion or smoldering (Figs. 8b,d) using an experimental algorithm that employs dynamic MIR and TIR thresholds derived from observations of Californian wildfires with the airborne Autonomous Modular Sensor (e.g., Ambrosia and Wegener 2009; Peterson and Wang 2013; Peterson et al. 2013, Schroeder et al. 2014). Saturated fire pixels are always considered as a subset of the flaming class, because they likely contain a significantly large flaming fraction (Thapa et al. 2021, manuscript submitted to *Nat. Commun. Earth Environ.*).

Quantitative fire characteristics derived from this dataset (Table 2) provide the first opportunity to validate fire modeling results in previous studies, which suggest that an expansive flaming region, specific fire front geometry, substantial available fuel, and a large heat flux are required to initiate and sustain pyroCb activity (e.g., Zhang et al. 2019; Badlan et al. 2021a,b). During the first MASTER overpass (Figs. 8a,b), all three of the fire updraft regions contributing to pyroCb development coincided with a combined flaming and smoldering area ranging from 1.4 km^2 at the northern updraft region to 3.3 km^2 at the southern region. Total FRP ranged from 1,013 to 605 MW at the southern and northern updraft regions, respectively. The flaming portion of the southern updraft region (2.3 km^2) was approximately 1,912 m long and 1,648 m wide (Fig. 8b). This fire geometry and large spatial expanse (e.g., length and deep flaming zone) has been hypothesized to generate a wide plume core that is less susceptible to entrainment and dilution with increasing altitude (Finney and McAllister 2011; McRae et al. 2015; Badlan et al. 2021a,b), explaining why the first two pyroCb pulses developed primarily over the southern updraft region. The stage was set by significant fire

Table 2. Quantitative fire and fuel characteristics from MASTER.

Variable	Units	Region 1 South	Region 2 Middle	Region 3 North	Region 3 (Pass 2) North
Smoldering area	km^2	1.0	0.8	0.4	0.6
Flaming area[a]	km^2	2.3	2.0	1.0	1.6
Total area	km^2	3.3	2.8	1.4	2.2
Smoldering total FRP	MW	217	143	87	134
Flaming total FRP[a]	MW	796	1,042	518	1,038
Total FRP	MW	1,013	1,185	605	1,172
Smoldering FRP-to-area ratio	$W\ m^{-2}$	217	179	218	223
Flaming FRP-to-area ratio[a]	$W\ m^{-2}$	346	521	518	649
Total FRP-to-area ratio	$W\ m^{-2}$	307	423	432	533
Smoldering fuel	tC	460	717	461	707
Flaming fuel[a]	tC	1,742	2,785	1872	2,875
Total fuel	tC	2,201	3,502	2,333	3,582
Smoldering consumption rate	$tC\ km^{-2}$	453	870	1,257	1,174
Flaming consumption rate[a]	$tC\ km^{-2}$	748	1,399	1,838	1,782
Total consumption rate	$tC\ km^{-2}$	659	1,244	1,683	1,616
Smoldering pixels	Count	7,524 (64%)	6,015 (54%)	2,791 (54%)	5,449 (55%)
Flaming pixels	Count	4,269 (36%)	4,817 (44%)	2,287 (44%)	4,030 (41%)
Saturated pixels	Count	29 (0.2%)	221 (2%)	102 (2%)	389 (4%)

[a] Flaming includes pixels with saturated FRP.

activity in this region earlier in the day (Fig. 3). While the flaming portion of the northern region (1.0 km^2) was comparatively narrower on its shortest axis (786 m), it was still wide enough to support a plume capable of generating large pyroCu in the ambient thermodynamic environment (Figs. 1 and 5a,b).

Dividing total FRP by the flaming and smoldering areas in each updraft region provides an FRP-to-area ratio that effectively distinguishes large fires burning at low intensities from smaller fires burning at high intensities (Peterson and Wang 2013; Peterson et al. 2013, 2014). During the first MASTER overpass, the northern and middle updraft regions of Williams Flats coincided with the largest FRP-to-area ratio from flaming pixels (518–521 $W\ m^{-2}$) and from the combined flaming and smoldering area (423–432 $W\ m^{-2}$). The southern updraft region coincided with the smallest FRP-to-area ratios despite a larger fire area (346 $W\ m^{-2}$ flaming, 307 $W\ m^{-2}$ total). These FRP-to-area ratios reveal that the northern and middle fire updraft regions were the most vigorous, and thus produced the largest smoke plume thermal buoyancy (Lavoué et al. 2000; Kahn et al. 2007), likely explaining why pyroCb development shifted from the southern to northern portion of the fire front after this short transition phase (Table 1). The second MASTER overpass at the northern updraft region (Figs. 8c,d; 44 min later) reveals that total FRP, fire area, and FRP-to-area ratio increased, with the FRP-to-area ratio from flaming pixels increasing by 131 $W\ m^{-2}$. The width of the flaming portion also increased by approximately 337 m, and the fire front by 564 m (Fig. 8d). The third, and most intense, pyroCb pulse developed over this northern portion of the fire during the 44-min time interval between MASTER overpasses (Figs. 5b,c), suggesting that relatively small changes in fire characteristics can have a significant impact on the magnitude and duration of pyroCb activity, especially in a thermodynamic environment that is generally favorable for intense burning and convective development (Fig. 1). While recently developed pyroCb predictive tools consider the overarching thermodynamic environment (Tory and Kepert 2021; Leach and Gibson 2021), they are unable to account for this variation in localized fire characteristics.

The remotely sensed FRP-to-area ratios at Williams Flats (300–650 W m^{-2}) are comparable with those observed for other fires during FIREX-AQ (490–590 W m^{-2}; Thapa et al. 2021, manuscript submitted to *Nat. Commun. Earth Environ.*). These figures based on remote sensing are smaller than estimates of sensible heat flux from previous fires in the western United States (e.g., 87 kW m^{-2}; Lareau and Clements 2017) and those used in idealized modeling of pyroCb development (25–100 kW m^{-2}; Badlan et al. 2021a,b). While sensible heat is a major contributor to retrieved FRP, the FRP-to-area ratios from MASTER do not provide a direct comparison. This is partly because the power-law distribution of fire energy release (Kumar et al. 2011) means that individual pixel values integrated over a large fire front primarily sample areas much less active than areas represented by sensible heat flux estimates. Smoke plume modeling studies have parameterized sensible heat as a function of FRP per pixel (Iguchi et al. 2018). Application of these methods to the full range of FRP from MASTER pixels in all fire severity rankings (0.0052–6.7 MW; Figs. 8a,c) provides an instantaneous, estimated sensible heat flux range from 30 kW m^{-2} to 40 MW m^{-2}. Understanding the relationships between remotely sensed and ground-level measurements of fire energetics remains a key research priority involving field measurements, as well as aircraft and satellites.

Fuel type and energy released

Information on fuel consumption during pyroCb development and the resulting impact on smoke plume chemistry in the UTLS remains almost entirely unconstrained. While the majority of pyroCbs are linked to large fires burning in forest or mixed forest and chaparral vegetation (Peterson et al. 2017a,b), a few have occurred in regions with significantly less fuel, such as the Texas Panhandle (e.g., Zhang et al. 2019). FIREX-AQ provides a unique opportunity to advance this science by combining a high-resolution fuels dataset with the remotely sensed fire characteristics from MASTER. Fuels data were obtained from the 30-m Fuel Characteristic Classification System (FCCS, uncertainty 26%) developed in previous studies (Ottmar et al. 2007; Prichard et al. 2019), providing 38 unique fuel types for Williams Flats. Fuel consumption was calculated for five fire-severity categories for each of the three fire updraft regions using fuel decision tables developed for FIREX-AQ (Kasischke et al. 1995; Conard and Ivanova 1997; Soja et al. 2004). Each category was based on quintiles of the 30-m FRP dataset (Figs. 8a,c, Fig. ES1). The amount of fuel consumed in each of these five categories is dependent on the amount of fuel contained in the FCCS data and the WFAS fire danger class, which relates meteorology to the relative dryness of fuels and their availability to burn (Deeming et al. 1977; Bradshaw et al. 1984).

On 8 August 2019, hot temperatures, low relative humidity, wind speed, and the slope of the landscape aligned to promote very active burning at the Williams Flats fire. This resulted in active forest-crown torching, short-range spotting, and rapid uphill runs on forested landscapes (Johnson 2019). Figure 9 shows the total fuels burned at each of the three fire updraft regions for both MASTER observation times. The 38 possible fuel types from FCCS are grouped into five broader categories, revealing that the primary fuel type burned in each region was forest. This suggests that dense fuels are required to sustain the expansive flaming areas within each updraft region. However, the southern updraft region burned a substantial amount of grasslands in terms of area. Chemistry of high-altitude smoke exhaust may therefore exhibit differences between the pyroCb pulses driven by the southern updraft region (pulses 1 and 2) and northern region (pulse 3; Table 1), which were separated by approximately 13 km (Fig. 5a).

Table 2 provides a summary of fuel consumed by smoldering and flaming combustion for each of the three updraft regions. As expected, the largest fuel consumption occurred with the largest FRP-to-area ratios from flaming combustion, which were the highest for the densely forested northern updraft region as the third pyroCb pulse developed. The rate of fuel consumption was the smallest in the southern region (659 tC km^{-2}), which reached a maximum

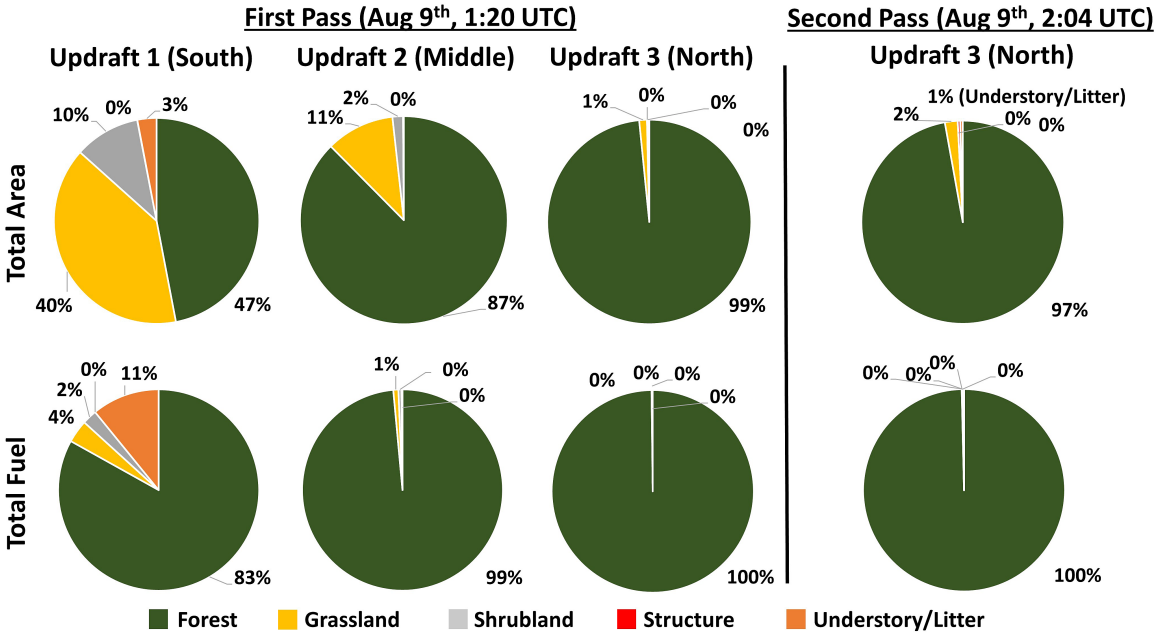

Fig. 9. Fuel Characteristic Classification System (FCCS) fuel beds. (top) The primary FCCS fuels on the landscape in the area delineated by MASTER data during the Williams Flats fire on 9 Aug 2019 (8 Aug LT). (bottom) The total fuels consumed, based on MASTER burned area, FCCS fuel beds, and Wildland Fire Assessment System (WFAS) fire danger ratings.

intensity before the DC-8 arrived, and the rate of consumption was nearly twice as high in the middle updraft region (1244 tC km^{-2}), coinciding with an active and growing fire front. The largest rates of fuel consumed coincided with the northern updraft region during both MASTER observations (1683 and 1616 tC km^{-2}). These are the first fuel estimates that link active fire fronts to the fuels that act to promote pyroCb activity in an atmosphere that is conducive to drying fuels and providing the thermodynamics necessary for pyroCb development.

The energy released by the three fire updraft regions was estimated by multiplying the total mass of fuel consumed by an assumed effective heat of combustion of 18,700 kJ kg^{-1} (Rosenfeld et al. 2007; Peterson et al. 2021). Energy release ranged from 4.1×10^7 to 6.7×10^7 MJ at the southern and northern updraft regions, respectively. The total energy released by all three updraft regions was 2.2×10^8 MJ. While this is a significant amount of energy release to drive pyroCb development, it is much smaller than the energy release estimated for other significant pyroCb events (10^9–10^{11} MJ) that ultimately injected large smoke plumes into the stratosphere (Fromm et al. 2006; Rosenfeld et al. 2007; Peterson et al. 2021). The relative roles of preceding fire weather, fuel amount and structure, and atmospheric thermodynamics in pyroCb development can therefore exhibit significant variation across the full spectrum of pyroCb activity observed worldwide.

Weather radar observations

Ground-based weather radar observations (S-band, WSR-88D) at Spokane, Washington (KOTX), were employed using the Gibson Ridge Level II Analyst (v. 2.50) radar-viewing application (http://www.grlevelx.com) to track the development and evolution of each pyroCb pulse originating from the three fire updraft regions (Table 1). The Williams Flats fire was located only ~65 km from the radar site, providing a fortuitous opportunity to supplement airborne measurements from the DC-8 with a variety of radar-derived variables. A radar animation for the entire Williams Flats pyroCb event is available in the supplemental material. It applies a 5.0° tilt angle (5–6 km above ground level), which is above the pyroCb LCL (Fig. 1). A vertical cross section based on the radar volume scan for the northern updraft region (Fig. 10) highlights a large and rapid increase in reflectivity (10–20 dBZ) between the initial pass over the

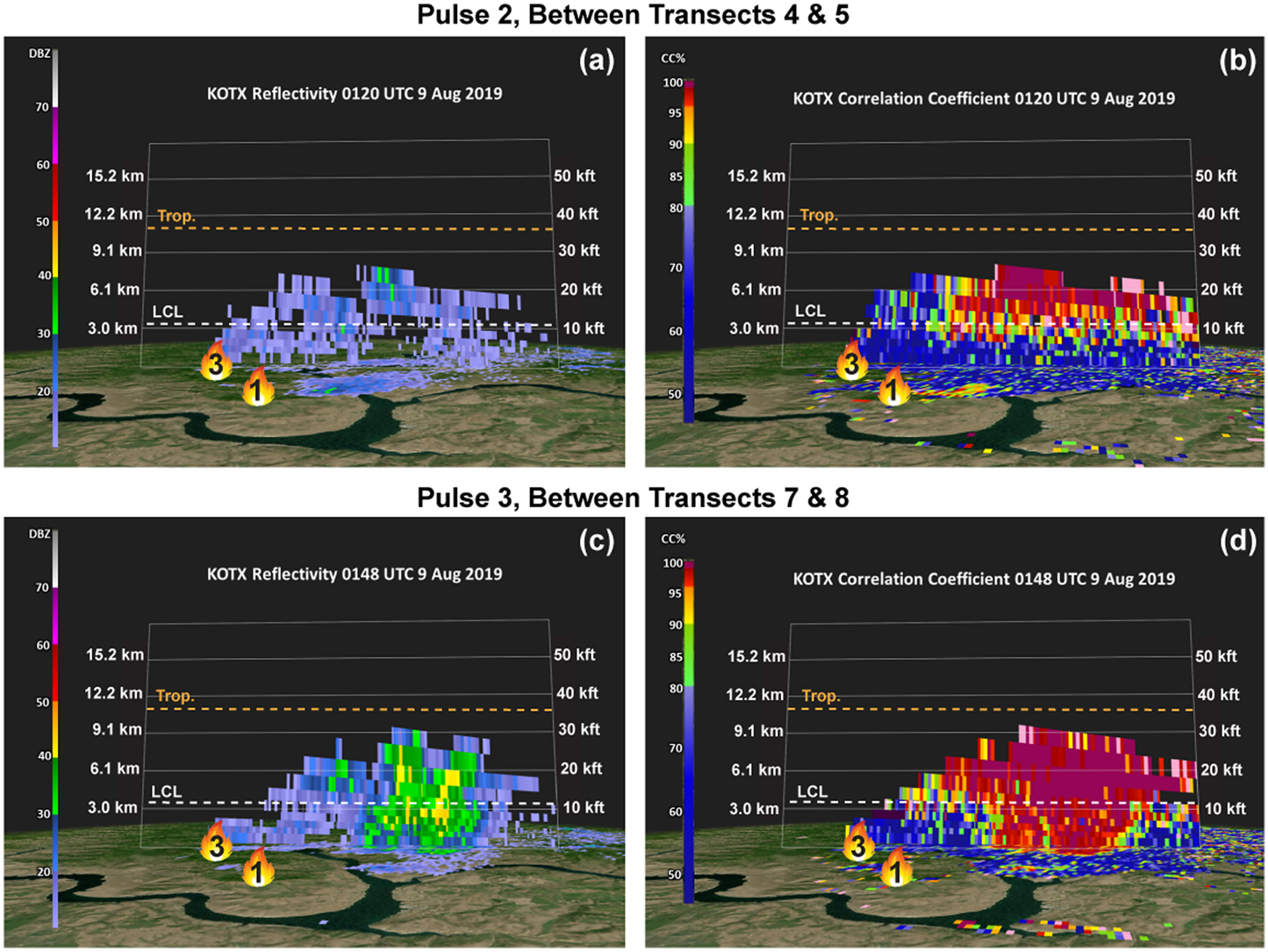

Fig. 10. KOTX radar volume cross-section panels of (a),(c) reflectivity and (b),(d) correlation coefficient over the northern portion of the Williams Flats fire (updraft 3) for two separate time periods on 9 Aug 2019 (8 Aug LT) using the Gibson Ridge Level II Analyst (v. 2.50) radar-viewing application (http://www.grlevelx.com). Vertical coordinate is altitude above ground level. The pyroCb lifting condensation level (LCL) and tropopause altitudes are marked by dashed white and orange lines, respectively.

fire (0121 UTC; Figs. 5a and 8a,b) and peak intensity of the third pyroCb pulse (0149 UTC). Maximum echo-top altitude also increased from approximately 7.6 km (25,000 ft) to more than 9.0 km (30,000 ft) during this time interval.

Dual polarization technology allows cloud droplets and ice (hydrometeors) to be distinguished from large, scattering fire debris (pyrometeors) using correlation coefficient (CC), which provides the correlation between the vertical and horizontal polarizations in a value from zero to one (Kumjian 2013). Pyrometeors generally have a CC below 0.6 due to the varied vertical and horizontal dimensions of large fire debris, while hydrometers have a CC close to 1.0 due to the homogeneity of ice and liquid particles (Lang et al. 2014; McCarthy et al. 2019). The radar cross section at 0121 UTC shows the third pyroCb pulse developing in the midtroposphere (high CC) over an underlying layer of smoke, ash, and other debris (low CC). By 0149 UTC, radar echoes with higher reflectivity values (>30 dB*Z*) and large CC (>0.95) descended below the LCL into the low-level smoke layer near the center of the cross section, suggesting that precipitation was generated by the pyroCb and may have reached the surface. Lightning flashes were detected by the *GOES-17* Geostationary Lightning Mapper (GLM) during this same time period (Fig. 6c). However, the pyroCb

downdraft was located several kilometers downwind of the fire in a remote region with no ground-based observations to verify precipitation occurrence. The horizontal distance between updraft and downdraft resulted from vertical wind shear between the surface (~10 kt) and the jet stream injection altitude (30–50 kt; Fig. 1). Downdraft characteristics were also likely influenced by a delay in precipitation development from aerosol indirect effects (e.g., Rosenfeld et al. 2008, 2014).

Cloud microphysical properties

When compared with typical thunderstorms, pyroCbs are characterized by smaller cloud droplet and ice particle size distributions (Reutter et al. 2014; Chang et al. 2015; Kablick et al. 2018), resulting from the large quantity of smoke particles that dominate nucleation, condensation, and freezing processes (Rosenfeld et al. 2007; Jahn et al. 2020). However, the Williams Flats pyroCb activity was smaller in magnitude than the large events analyzed previously. Echo tops (Fig. 10) only extended about a kilometer above the level of homogeneous freezing (from −35° to −40°C; Rosenfeld et al. 2007; Peterson et al. 2017a,b) during peak intensity, allowing cloud processes to be influenced by a warmer, mixed-phase temperature regime. Measurements of cloud microphysical properties during FIREX-AQ therefore provide an opportunity to compare a pyroCb injecting smoke into the upper troposphere with previously analyzed cases of direct smoke injection into the lower stratosphere.

A second-generation Cloud, Aerosol and Precipitation Spectrometer (CAPS; Spanu et al. 2020) and a Precipitation Imaging Probe (PIP) were mounted under the wing of the NASA DC-8. These wing-probe instruments measured the size and shape of aerosol and cloud particles in the nominal particle diameter range from 0.5 to 6200 μm at ambient conditions. Particles were captured up to a diameter of 50 μm by the Cloud and Aerosol Spectrometer (CAS), which is the optical spectrometer part of CAPS. To derive representative number size distributions from optical spectrometers like CAS, assumptions have to be made on the refractive index of the measured particles. For the presented sequences of the FIREX-AQ dataset, refractive indices representing organic aerosol particles were used up to a particle diameter of 3 μm. The refractive index of ice was used for larger sizes. The second part of the CAPS, the Cloud Imaging Probe (CIP), is an optical array probe recording shadow images of the aerosol and cloud particles in the size range between 15 and 930 μm. The PIP is also an optical array probe covering the size range between 100 and 6200 μm.

Figure 11 provides log number size distributions derived from the combined measurement ranges of the two instruments, along with a sample of the corresponding particle imagery. These include a detached pyroCb anvil (Fig. 4c; pulse 1, transect 2), upper portion of an active pyroCb (pulse 2, transect 4), and a lower sampling altitude within an active pyroCb (mix of pulses 2 and 3, transect 8). All three transects coincided with 500–1800 ppbv of CO (Fig. 4c), thus confirming smoke presence. The corresponding particle size distributions contain a large quantity (>100 cm^{-3}) of particles near the minimum detection limit of 0.5 μm (CAS instrument). This overlaps the upper portion of the expected fine mode diameter size range for fresh biomass burning smoke particles in the midlatitudes (0.1–0.5 μm; Reid et al. 2005a) and the approximate size range measured in aged UTLS smoke plumes (0.2–0.8 μm; Ditas et al. 2018), including the lower portion of the size range measured in the stratospheric Chisholm pyroCb plume 2 months after injection (0.6–1.2 μm; Fromm et al. 2008b). It is possible that coarse mode ash particles (2.5–15-μm diameter) and significantly larger fire debris were also pulled upward in the pyroCb updraft, as evidenced by the presence of large pyrometeors (low CC values) in weather radar echoes below cloud base (Fig. 10).

Higher-altitude (anvil-top) size distributions from −31° to −40°C (Figs. 11a,b) exhibit a local maximum at 10–50 μm, which coincides with particle diameters derived from remote sensing

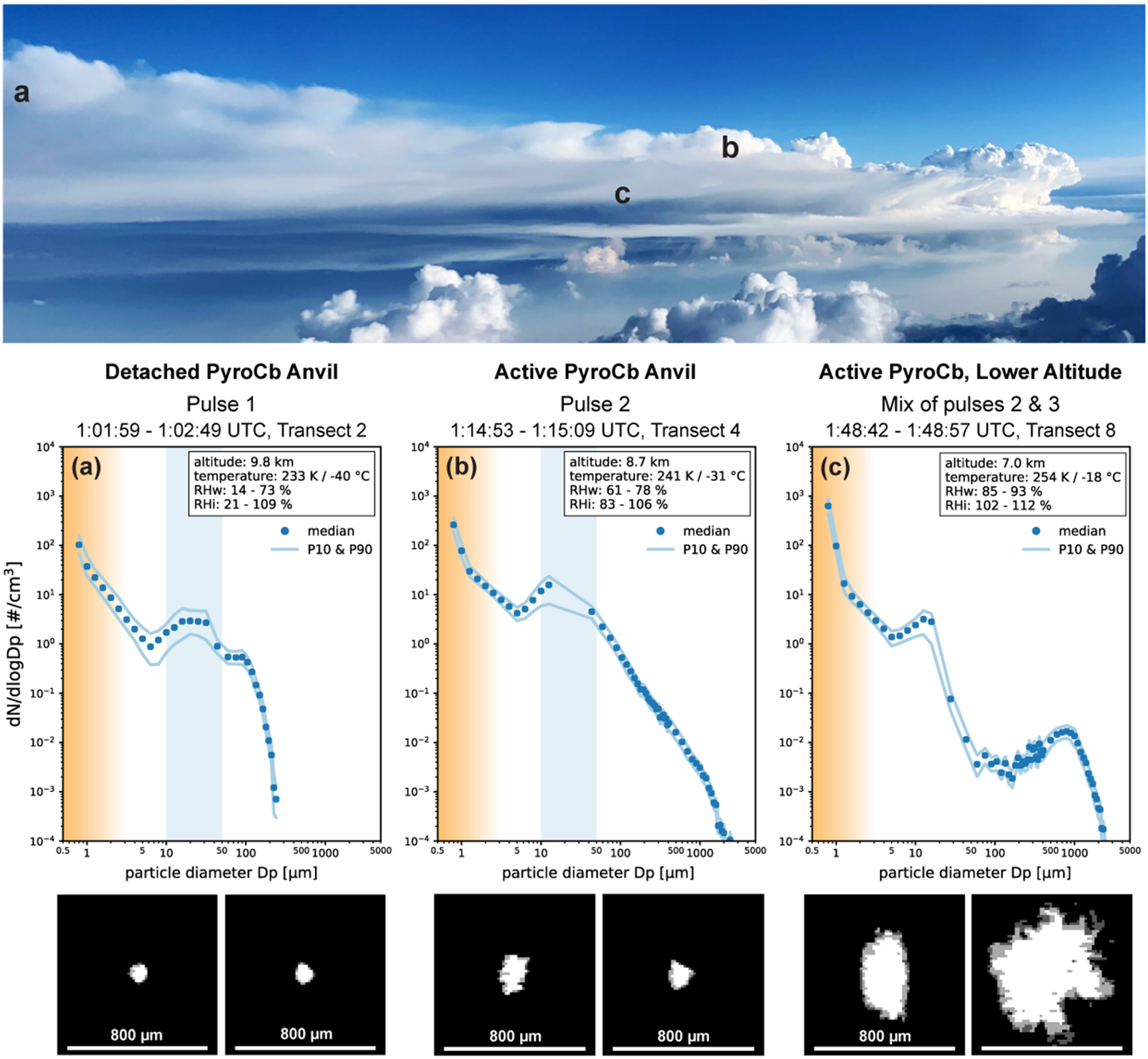

Fig. 11. Combined particle log number size distributions at standard pressure and temperature conditions (1013 hPa, 273.15 K) derived from measurements with wing-probe instruments CAPS and PIP for transects within (a) detached pyroCb anvil, (b) upper portion of an active pyroCb, and (c) lower sampling altitude within an active pyroCb. Calculated uncertainty and variability of each transect are illustrated with blue dots and solid lines representing median and percentiles, respectively. Average values for aircraft altitude, ambient temperature, and relative humidity over ice and water of each transect are included in the legend. Brown shading depicts the aerosol size range, including the transition to cloud particles. Blue shaded areas between 10 and 50 μm indicate particle diameters inferred from remote sensing observations of the Chisholm fire pyroCb anvil in 2001 (Rosenfeld et al. 2007). Single particle images are selections of CIP recordings of each size distribution. The pyroCb side-view photo (0144 UTC, pulse 3) provides a basic visual reference for the approximate measurement location of the three size distributions.

observations in the ice anvil clouds of large pyroCbs, such as the Chisholm event in 2001 (Rosenfeld et al. 2007). However, larger particle sizes (>100 μm) are also present, especially within the active pyroCb cloud tops (Fig. 11b). These relatively large particle sizes deviate from the assumed small ice properties of a pyroCb anvil that serve as the basis for pyroCb detection from satellite observations, explaining why a previously developed pyroCb detection

algorithm (Peterson et al. 2017b) failed to detect any pyroCb activity over Williams Flats. Size distributions obtained approximately 1,700 m lower within the active pyroCb at −18°C (Fig. 11c) are bimodal within the cloud particle range, exhibiting a local maximum around 1,000 μm (1 mm). The presence of large ice particles is indicative of precipitation-forming processes within the pyroCb (e.g., Rosenfeld and Gutman 1994; Rosenfeld et al. 2007, 2014), which is further supported by the presence of hydrometers below the cloud base (high CC values) in Fig. 10. These lower-altitude cloud particle size measurements were also coincident with lightning initiation over Williams Flats (Fig. 6c, pulse 3).

When compared with intense pyroCb events, the relatively larger particle sizes and potential precipitation associated with the Williams Flats pyroCb activity support enhanced scavenging of smoke particles. This result may partially explain the lack of an expansive smoke plume detectable in the upper troposphere following the event. Jet stream winds also played a role in diffusing the smoke exhaust as it was rapidly transported downwind. The magnitude of smoke injection from pyroCb activity may therefore depend on a feedback loop, where stronger pyroCb updrafts result in a shift toward smaller ice particle size distributions (induced by rapid homogeneous freezing of droplets) that reduce the chance for significant precipitation scavenging, ultimately facilitating rapid vertical smoke transport and efficient exhaust through the high-altitude anvil region, which can reach the stratosphere. Smaller pyroCb events, such as Williams Flats, likely coincide with relatively weaker updrafts, lower injection altitudes, and larger cloud particle size distributions that reduce vertical smoke transport efficiency to some degree. All pyroCb events are anchored directly to a fire updraft region (plume core), and are therefore more efficient at transporting smoke to the UTLS than traditional thunderstorms of similar scale, rooted in a smoky boundary layer (Fromm et al. 2019).

Aerosol physical and optical properties

The bulk physical and optical properties of smoke particles from temperate and boreal forest fires have been extensively studied (e.g., Reid et al. 2005a,b; Akagi et al. 2011; Laing et al. 2016; Andreae 2019; Bian et al. 2020; Kleinman et al. 2020). However, particles lofted by pyroCb updrafts are transported to the UTLS through a combination of ice-phase or mixed-phase cloud processes, which will likely alter the effective smoke particle properties significantly from their ground-level values (Dahlkötter et al. 2014). Current methods for quantifying the impact of pyroCb activity on UTLS aerosol loading rely on assumed optical properties to convert satellite observations of individual plumes into smoke particle mass (Fromm et al. 2008a, 2021; Peterson et al. 2018, 2021). Aerosol property information is also required to simulate pyroCb plume transport, evolution, and radiative impacts (e.g., Yu et al. 2019, 2021; Christian et al. 2019; Das et al. 2021). The comprehensive, in situ aerosol physical and optical property measurements obtained during FIREX-AQ provide the first opportunity to validate and calibrate these methods and modeling applications.

Aerosol optical properties for the Williams Flats pyroCb event are limited to the first five transects due to an inlet sampling malfunction that occurred midflight (just before 0130 UTC). Each transect was sorted into samples from the downwind, detached anvil (pulse 1, approximate smoke age of 2 h) and samples from the second developing/active anvil (pulse 2, smoke age of 10–60 min). Figure 12a provides 1-s data from the Langley Aerosol Research Group (LARGE) in situ measurements of single scattering albedo (SSA) measured at 550 nm (Ziemba et al. 2013). SSA is the ratio of the aerosol scattering coefficient to the aerosol extinction coefficient, and thus quantifies the contribution of scattering and absorption to the overall particle light extinction. The Williams Flats pyroCb plume exhibited SSA values with an interquartile range (IQR) of 0.94–0.96 in the active anvil and 0.96–0.97 in the detached anvil, implying that the majority of particle extinction in this young pyroCb plume results from scattering. These SSA values in the upper troposphere are similar to those obtained from

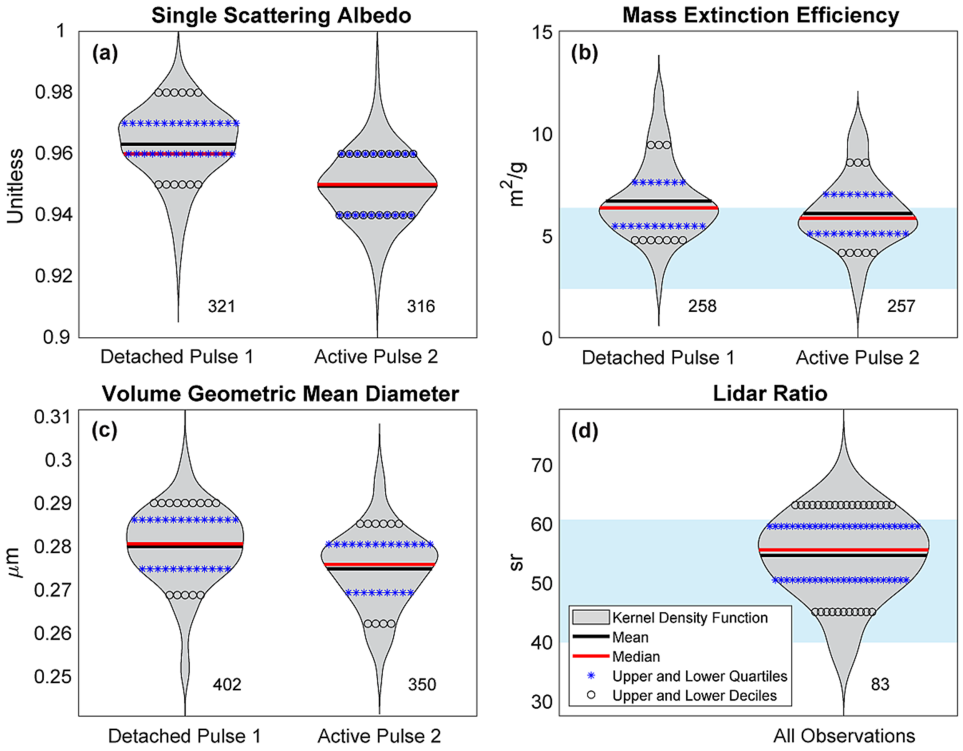

Fig. 12. Distributions of pyroCb smoke plume physical and optical properties displayed as violin plots, including (a) single scattering albedo, (b) mass extinction efficiency, (c) volume geometric mean diameter, and (d) lidar ratio. These plots include the mean (red solid line), median (black solid line), interquartile range (blue stars), and 10th–90th percentile range (black open circles). The shape of the gray shaded region represents the relative density of samples at each value, with a wider shaded region indicating a larger proportion of the total number of samples at a given value. The total number of samples is provided to the right of each violin plot. Blue shading indicates the range of mass extinction efficiency and lidar ratio employed in previous studies of large stratospheric smoke plumes injected by pyroCb activity in North America.

LARGE at lower altitudes in the young plume from the 2013 Rim Fire in California (Yu et al. 2016). Remotely sensed data for a large stratospheric plume 1–3 weeks after extreme pyroCb activity Canada (Pacific Northwest Event, 12 August 2017) reveal comparatively lower SSA (0.80–0.85; Das et al. 2021), indicating a much greater contribution of absorption to aerosol light extinction.

Mass extinction efficiency (MEE; Fig. 12b) is defined as the ratio between aerosol extinction and total aerosol mass. This quantity was derived at 532 nm using 1-s LARGE extinction data and 1-s high-resolution time-of-flight aerosol mass spectrometer (AMS) speciated mass data (DeCarlo et al. 2006). Total aerosol mass in the pyroCb plume was approximated by the sum of the organic sulfate, nitrate, ammonium, and chloride aerosol masses. The resulting MEE within the active pyroCb anvil coincided with an IQR of 5.1–7.4 $m^2\ g^{-1}$, which increased to 5.6–8.6 $m^2\ g^{-1}$ within the older, detached anvil. These values are higher than those reported by previous studies for lower altitude smoke in temperate and boreal regions (e.g., Reid et al. 2005b). The observed range also exceeds the assumed MEE upper bound employed to estimate smoke particle mass in the lower stratosphere approximately 12–72 h after pyroCb cessation (3.0–6.0 $m^2\ g^{-1}$; Peterson et al. 2018, 2021).

Figure 12c provides the geometric mean diameter of the aerosol number concentration (average size of aerosol particles in the pyroCb outflow) measured by the LARGE Laser Aerosol Spectrometer (LAS; Moore et al. 2021). LAS measurements include particle diameters smaller than 4–5 μm (McNaughton et al. 2007; Chen et al. 2011), which effectively extends the lower bound of the size range provided by the cloud probe instrumentation (Fig. 10). Mean particle

diameters in the pyroCb outflow were near 0.28 μm, with an active anvil IQR of 0.27–0.28 μm and a detached anvil IQR of 0.28–0.29 μm. These values are higher than those measured in fresh boundary layer smoke from Williams Flats (IQR 0.18–0.19 μm), as well as values from previous experiments involving boundary layer smoke (0.10–0.16 μm; Alonso-Blanco et al. 2012; Portin et al. 2012). MEE increases with aerosol mean diameter (Laing et al. 2016), thus explaining why the pyroCb smoke MEE exceeded the upper bound of previously used values. This highlights the importance of accounting for changes in aerosol physical and optical properties induced by rapidly processing a large quantity of smoke through a pyroCb cloud.

A key method for estimating stratospheric smoke particle mass employs the conversion of lidar backscatter (532 nm) into particle mass density using an assumed extinction-to-backscatter lidar ratio applied to satellite lidar observations (e.g., CALIOP; Peterson et al. 2018, 2021). Figure 12d provides a lidar ratio distribution (532 nm) for the Williams Flats pyroCb event measured at altitudes above 8 km by the DIAL-HSRL (Fig. 4d; Hair et al. 2008), which may not provide an exact spatial match with in situ smoke measurements (Figs. 4c,d). Lidar ratios were measured in regions of elevated backscatter (>1.7 mm^{-1} sr^{-1}) and lower depolarization (<0.2), which are more consistent with pyroCb-influenced smoke rather than ice. The IQR of these lidar ratios (49.8–58.6 sr) falls within the assumed range (40–60 sr) employed in a remote sensing study that quantified stratospheric smoke particle mass within 48 h of the 2017 Pacific Northwest Event in Canada (Peterson et al. 2018). However, lidar ratios exceeding 70 sr were reported in the same plume several days to weeks after injection, well downwind of North America (e.g., Ansmann et al. 2018; Haarig et al. 2018). This emphasizes the importance of understanding processes influencing pyroCb smoke transport and aging in the UTLS.

Aerosol and gas-phase chemistry

The DC-8 FIREX-AQ payload contained a large suite of instrumentation designed to measure aerosol and gas-phase chemistry of wildfire smoke. A summary is provided in Tables ES2 and ES3. These data are expected to address several additional unknowns in understanding the impact of pyroCb activity on UTLS chemistry. For example, one key unknown is the chemical composition of pyroCb anvils relative to traditional convective outflow. The time series in Fig. 4c reveals CO levels exceeding 1200 ppbv within the pyroCb activity sampled by FIREX-AQ. These values are an order of magnitude higher than those measured in high-altitude convective outflow during the Deep Convective Clouds and Chemistry (DC3) field campaign in 2012 (Barth et al. 2015), including a traditional thunderstorm that ingested smoke from a nearby wildfire (100–120 ppbv; Apel et al. 2015). The CO values measured within the Williams Flats pyroCb outflow were closer to those measured directly within the smoke plume during DC-3. This analysis further supports previous studies (e.g., Fromm et al. 2019) that describe pyroCb activity as an efficient vertical transport pathway for smoke to rapidly reach the UTLS. Future studies will explore additional unknowns, such as secondary aerosol production after smoke injection into the UTLS, which is likely a key factor influencing changes in smoke plume mass and evolution during the weeks and months following a large pyroCb event. In situ chemistry measurements are also essential for improved understanding of photochemical reactions in pyroCb plumes that influence ozone chemistry in the stratosphere (Yu et al. 2019), and host of other potential impacts, including interactions between pyroCb smoke and volcanic sulfate plumes (Peterson et al. 2021).

Summary and outlook

This study examined a unique set of in situ and remotely sensed measurements obtained before and during a pyroCb event over the Williams Flats fire in Washington State as part of the 2019 FIREX-AQ field experiment. NASA's DC-8 Flying Laboratory operated in the upper

troposphere, within the upper portion of three ice-capped convective columns, or pyroCb pulses. A wide variety of in situ measurements were obtained in 11 transects that include active pyroCb cloud tops, fresh smoke outflow immediately downwind of the fire, and a detached pyroCb anvil 80–100 km downwind. Cloud probe measurements, airborne lidar, and ground-based weather radar provided additional information on pyroCb evolution, injection altitude, and cloud microphysical properties. This FIREX-AQ dataset provides the first opportunity to connect meteorology, fuels, fire-line geometry, and fire radiative power to pyroCb development and cloud property evolution, including chemistry of the ensuing smoke exhaust in the upper troposphere.

The MODIS/ASTER Airborne Simulator (MASTER) obtained a high-resolution (~30 m) view of the fire characteristics during this pyroCb event, revealing that three plume cores along distinct regions of the fire front (fire updraft regions) contributed to pyroCb development. Each updraft region primarily burned dense forest fuel types, but the southern updraft region included some grasslands, which likely influenced chemistry of the ensuing pyroCb smoke exhaust. Quantitative fire characteristics from MASTER showed that pyroCb development can result from lower energy fires when the preceding meteorology supports drying of fuels and the coincident thermodynamic environment is supportive of convective development. Comparisons between two MASTER overflights identified rapid changes in fire geometry and spatial expanse (e.g., deep flaming zone) that dramatically influenced the magnitude, behavior, and duration of pyroCb activity. An additional remote sensing payload on board NASA's ER-2 aircraft identified the start of a localized fire spread event approximately 6.5 h earlier, which ultimately set the stage for pyroCb development. This combined dataset serves as the first validation for previous idealized modeling of fire and vegetation characteristics driving pyroCb development (e.g., Badlan et al. 2021a,b; Zhang et al. 2019). It also motivates examination of recently developed pyroCb prediction tools (Tory and Kepert 2021; Leach and Gibson 2021) to understand their efficacy in situations featuring multiple fire fronts with varying geometry. Future applications include improved simulation of pyroCb activity in fine-scale models of fire–weather interaction (e.g., Coen et al. 2018, 2020; Kochanski et al. 2019) and convection-allowing numerical weather prediction (e.g., Evans et al. 2018) to ultimately quantify the relative roles of fuel amount and structure, fire energy and geometry, and meteorology in pyroCb development.

Ground-based weather radar observed large and rapid increases in reflectivity and echo-top altitudes coincident with changes in fire characteristics. The presence of large ice particles within the pyroCb and hydrometers below the cloud base altitude indicated that precipitation was generated by this event. The resulting feedbacks likely enhanced smoke particle scavenging and reduced vertical transport efficiency when compared with intense pyroCb events that reached the lower stratosphere. PyroCb microphysical properties measured by FIREX-AQ will be employed in future studies to improve radiative transfer modeling and remote sensing applications required to detect and monitor pyroCb events in real time (Peterson et al. 2017b). These measurements can be applied to advance current understanding of lightning in pyroCb activity (e.g., Rosenfeld et al. 2007; Lang et al. 2014; LaRoche and Lang 2017) and aviation safety near these unique storms (Rodriguez et al. 2020).

The FIREX-AQ dataset also includes the first in situ measurements of aerosol physical and optical properties in a young pyroCb plume, which are essential for constraining existing estimates of smoke particle mass injected into the lower stratosphere. The observed lidar ratios fell within the range of assumed and derived values used in previous studies, but the observed mass extinction efficiency (MEE) exceeded the upper bound of previous assumptions. A large suite of aerosol and gas-phase chemistry measurements confirmed that all pyroCb activity, regardless of magnitude, serves as an efficient vertical smoke transport pathway, especially when compared with similar measurements taken in traditional thunderstorms during

previous experiments. These data will be employed in future studies to validate and refine assumptions currently employed in numerical modeling studies to ultimately understand the role of pyroCb smoke plumes in the climate system, including potential impacts on radiative forcing, dynamic circulation, and ozone chemistry in the stratosphere (e.g., Yu et al. 2019, 2021; Christian et al. 2019; Das et al. 2021).

While FIREX-AQ provided a significant advancement in the study of pyroCb activity and its impacts, additional airborne observational studies are required to examine smoke plumes ensuing from the full spectrum of pyroCb activity, including larger pyroCb events that inject smoke directly into the lower stratosphere (e.g., Peterson et al. 2018, 2021). Future studies must include repeated sampling of the same pyroCb plume over multiple days to understand its chemical evolution, similar to previous studies of lower-altitude smoke (e.g., Forrister et al. 2015; Kleinman et al. 2020; Hodshire et al. 2021). To improve predictive potential, these plumes should be explicitly linked to the fire characteristics (e.g., fuel amount and structure, geometry, and energy) that promote pyroCb development. Nighttime airborne measurements are required to validate recent advancements in nocturnal fire detection, estimates of combustion phase, and their potential application to pyroCb prediction (e.g., Polivka et al. 2016; Wang et al. 2020). When considering the extreme magnitude of recent pyroCb events observed worldwide (e.g., Peterson et al. 2018, 2021), there is a growing need for intensive field studies focused on extreme wildfires, pyroCb activity, and ensuing smoke plume impacts.

Acknowledgments. We thank Melinda Berman, Alexa Zabaske, Aaron Zeeb, and Maritza Arreola Amaya for their contributions to FIREX-AQ as part of the Naval Research Enterprise Internship Program (NREIP). We also thank Melinda Surratt and Mike Fromm at the Naval Research Laboratory and Fangjun Li of South Dakota State University for their helpful advice and assistance with satellite data processing. We are grateful for the contributions and support provided by the entire FIREX-AQ Science Team, especially Pedro Campuzano-Jost (University of Colorado Boulder), NASA Program Manager Barry Lefer, and Project Scientists Carsten Warneke, Joshua (Shuka) Schwarz, and Jack Dibb. NASA and NOAA supported this work under programs related to the FIREX-AQ Science Team (80HQTR18T0063, 80NSSC18K0685, 80NSSC18K0629, 80NSSC20K1650, NA18OAR4310107). Additional support for David Peterson was provided by NASA's New Investigator Program (80HQTR18T0073) and Modeling, Analysis, and Prediction (MAP) Program (80HQTR21T0099). Charles Ichoku acknowledges support from the NOAA Educational Partnership Program with Minority Serving Institutions (NOAA/EPP/MSI) under Agreement NA16SEC4810006. A portion of this research was supported by the European Research Council H2020 programme (Grant A-LIFE 640458). A portion of this research was carried out at the Jet Propulsion Laboratory, California Institute of Technology, under a contract with NASA.

Data availability statement. Data from all measurement platforms used in FIREX-AQ are archived at https://www-air.larc.nasa.gov/missions/firex-aq/ (DOI:10.5067/SUBORBITAL/FIREXAQ2019/DATA001). Photos of the observed pyroCb activity are available from the corresponding author upon request. Data from the GOES-17 ABI, including output from NOAA's Fire Detection and Characterization Algorithm, can be obtained from the NOAA Comprehensive Large Array-data Stewardship System (CLASS) at https://www.class.noaa.gov.

References

Abatzoglou, J. T., A. P. Williams, and R. Barbero, 2019: Global emergence of anthropogenic climate change in fire weather indices. *Geophys. Res. Lett.*, **46**, 326–336, https://doi.org/10.1029/2018GL080959.

Akagi, S. K., R. J. Yokelson, C. Wiedinmyer, M. J. Alvarado, J. S. Reid, T. Karl, J. D. Crounse, and P. O. Wennberg, 2011: Emission factors for open and domestic biomass burning for use in atmospheric models. *Atmos. Chem. Phys.*, **11**, 4039–4072, https://doi.org/10.5194/acp-11-4039-2011.

Allen, D. R., M. D. Fromm, G. P. Kablick III, and G. E. Nedoluha, 2020: Smoke With Induced Rotation and Lofting (SWIRL) in the stratosphere. *J. Atmos. Sci.*, **77**, 4297–4316, https://doi.org/10.1175/JAS-D-20-0131.1.

Alonso-Blanco, E., A. I. Calvo, R. Fraile, and A. Castro, 2012: The influence of wildfires on aerosol size distributions in rural areas. *Sci. World J.*, **2012**, 735697, https://doi.org/10.1100/2012/735697.

Ambrosia, V. G., and S. S. Wegener, 2009: Unmanned airborne platforms for disaster remote sensing support. *Geoscience and Remote Sensing*, P. P. Ho, Ed., IntechOpen, 91–114, https://doi.org/10.5772/8302.

Andreae, M. O., 2019: Emission of trace gases and aerosols from biomass burning – An updated assessment. *Atmos. Chem. Phys.*, **19**, 8523–8546, https://doi.org/10.5194/acp-19-8523-2019.

Ansmann, A., and Coauthors, 2018: Extreme levels of Canadian wildfire smoke in the stratosphere over central Europe on 21–22 August 2017. *Atmos. Chem. Phys.*, **18**, 11 831–11 845, https://doi.org/10.5194/acp-18-11831-2018.

Apel, E. C., and Coauthors, 2015: Upper tropospheric ozone production from lightning NOx-impacted convection: Smoke ingestion case study from the DC3 campaign. *J. Geophys. Res. Atmos.*, **120**, 2505–2523, https://doi.org/10.1002/2014JD022121.

Badlan, R. L., J. J. Sharples, J. P. Evans, and R. H. D. McRae, 2021a: Factors influencing the development of violent pyroconvection. Part I: Fire size and stability. *Int. J. Wildland Fire*, **30**, 484–497, https://doi.org/10.1071/WF20040.

——, ——, ——, and ——, 2021b: Factors influencing the development of violent pyroconvection. Part II: Fire geometry and intensity. *Int. J. Wildland Fire*, **30**, 498–512, https://doi.org/10.1071/WF20041.

Barth, M. C., and Coauthors, 2015: The Deep Convective Clouds and Chemistry (DC3) field campaign. *Bull. Amer. Meteor. Soc.*, **96**, 1281–1309, https://doi.org/10.1175/BAMS-D-13-00290.1.

Bian, Q. J., B. Ford, J. R. Pierce, and S. M. Kreidenweis, 2020: A decadal climatology of chemical, physical, and optical properties of ambient smoke in the western and southeastern United States. *J. Geophys. Res. Atmos.*, **125**, e2019JD031372, https://doi.org/10.1029/2019JD031372.

Bradshaw, L. S., J. E. Deeming, R. E. Burgan, and J. D. Cohen, 1984: The 1978 National Fire-Danger Rating System: Technical documentation. General Tech. Rep. INT-169, U.S. Department of Agriculture, 44 pp., https://doi.org/10.2737/INT-GTR-169.

Canadell, J. G., C. P. Meyer, G. D. Cook, A. Dowdy, P. R. Briggs, J. Knauer, A. Pepler, and V. Haverd, 2021: Multi-decadal increase of forest burned area in Australia is linked to climate change. *Nat. Commun.*, **12**, 6921, https://doi.org/10.1038/s41467-021-27225-4.

Chang, D., and Coauthors, 2015: Comprehensive mapping and characteristic regimes of aerosol effects on the formation and evolution of pyro-convective clouds. *Atmos. Chem. Phys.*, **15**, 10 325–10 348, https://doi.org/10.5194/acp-15-10325-2015.

Chen, G., and Coauthors, 2011: Observations of Saharan dust microphysical and optical properties from the Eastern Atlantic during NAMMA airborne field campaign. *Atmos. Chem. Phys.*, **11**, 723–740, https://doi.org/10.5194/acp-11-723-2011.

Christian, K., J. Wang, C. Ge, D. Peterson, E. Hyer, J. Yorks, and M. McGill, 2019: Radiative forcing and stratospheric warming of pyrocumulonimbus smoke aerosols: First modeling results with multisensor (EPIC, CALIPSO, AND CATS) views from space. *Geophys. Res. Lett.*, **46**, 10 061–10 071, https://doi.org/10.1029/2019GL082360.

Clements, C. B., N. P. Lareau, D. E. Kingsmill, C. L. Bowers, C. P. Camacho, R. Bagley, and B. Davis, 2018: The Rapid Deployments to Wildfires Experiment (RaDFIRE): Observations from the fire zone. *Bull. Amer. Meteor. Soc.*, **99**, 2539–2559, https://doi.org/10.1175/BAMS-D-17-0230.1.

Coen, J. L., E. N. Stavros, and J. A. Fites-Kaufman, 2018: Deconstructing the King megafire. *Ecol. Appl.*, **28**, 1565–1580, https://doi.org/10.1002/eap.1752.

——, W. Schroeder, S. Conway, and L. Tarnay, 2020: Computational modeling of extreme wildland fire events: A synthesis of scientific understanding with applications to forecasting, land management, and firefighter safety. *J. Comput. Sci.*, **45**, 101152, https://doi.org/10.1016/j.jocs.2020.101152.

Conard, S. G., and G. A. Ivanova, 1997: Wildfire in Russian boreal forests – Potential impacts of fire regime characteristics on emissions and global carbon balance estimates. *Environ. Pollut.*, **98**, 305–313, https://doi.org/10.1016/S0269-7491(97)00140-1.

Dahlkötter, F., and Coauthors, 2014: The Pagami Creek smoke plume after long-range transport to the upper troposphere over Europe – Aerosol properties and black carbon mixing state. *Atmos. Chem. Phys.*, **14**, 6111–6137, https://doi.org/10.5194/acp-14-6111-2014.

Das, S., P. R. Colarco, L. D. Oman, G. Taha, and O. Torres, 2021: The long-term transport and radiative impacts of the 2017 British Columbia pyrocumulonimbus smoke aerosols in the stratosphere. *Atmos. Chem. Phys.*, **21**, 12 069–12 090, https://doi.org/10.5194/acp-21-12069-2021.

DeCarlo, P. F., and Coauthors, 2006: Field-deployable, high-resolution, time-of-flight aerosol mass spectrometer. *Anal. Chem.*, **78**, 8281–8289, https://doi.org/10.1021/ac061249n.

Deeming, J. E., R. E. Burgan, and J. D. Cohen, 1977: The National Fire-Danger Rating System – 1978. General Tech. Rep. INT-39, U.S. Department of Agriculture, 63 pp.

Dennison, P. E., and D. A. Roberts, 2009: Daytime fire detection using airborne hyperspectral data. *Remote Sens. Environ.*, **113**, 1646–1657, https://doi.org/10.1016/j.rse.2009.03.010.

Di Virgilio, G., J. P. Evans, S. A. P. Blake, M. Armstrong, A. J. Dowd, J. Sharples, and R. McRae, 2019: Climate change increases the potential for extreme wildfires. *Geophys. Res. Lett.*, **46**, 8517–8526, https://doi.org/10.1029/2019GL083699.

Ditas, J., and Coauthors, 2018: Strong impact of wildfires on the abundance and aging of black carbon in the lowermost stratosphere. *Proc. Natl. Acad. Sci. USA*, **115**, E11595–E11603, https://doi.org/10.1073/pnas.1806868115.

Egorova, V. N., A. Trucchia, and G. Pagnini, 2020: Fire-spotting generated fires. Part I: The role of atmospheric stability. *Appl. Math. Modell.*, **84**, 590–609, https://doi.org/10.1016/j.apm.2019.02.010.

Evans, C., S. J. Weiss, I. L. Jirak, A. R. Dean, and D. S. Nevius, 2018: An evaluation of paired regional/convection-allowing forecast vertical thermodynamic profiles in warm-season, thunderstorm-supporting environments. *Wea. Forecasting*, **33**, 1547–1566, https://doi.org/10.1175/WAF-D-18-0124.1.

Finney, M. A., and S. S. McAllister, 2011: A review of fire interactions and mass fires. *J. Combust.*, **2011**, 548328, https://doi.org/10.1155/2011/548328.

Forrister, H., and Coauthors, 2015: Evolution of brown carbon in wildfire plumes. *Geophys. Res. Lett.*, **42**, 4623–4630, https://doi.org/10.1002/2015GL063897.

Fromm, M., and R. Servranckx, 2003: Transport of forest fire smoke above the tropopause by supercell convection. *Geophys. Res. Lett.*, **30**, 1542, https://doi.org/10.1029/2002GL016820.

——, and Coauthors, 2000: Observations of boreal forest fire smoke in the stratosphere by POAM III, SAGE II, and lidar in 1998. *Geophys. Res. Lett.*, **27**, 1407–1410, https://doi.org/10.1029/1999GL011200.

——, R. Bevilacqua, R. Servranckx, J. Rosen, J. P. Thayer, J. Herman, and D. Larko, 2005: Pyro-cumulonimbus injection of smoke to the stratosphere: Observations and impact of a super blowup in northwestern Canada on 3–4 August 1998. *J. Geophys. Res.*, **110**, D08205, https://doi.org/10.1029/2004JD005350.

——, A. Tupper, D. Rosenfeld, R. Servranckx, and R. McRae, 2006: Violent pyroconvective storm devastates Australia's capital and pollutes the stratosphere. *Geophys. Res. Lett.*, **33**, L05815, https://doi.org/10.1029/2005GL025161.

——, O. Torres, D. Diner, D. Lindsey, B. Vant Hull, R. Servranckx, E. P. Shettle, and Z. Li, 2008a: Stratospheric impact of the Chisholm pyrocumulonimbus eruption: 1. Earth-viewing satellite perspective. *J. Geophys. Res.*, **113**, D08202, https://doi.org/10.1029/2007JD009153.

——, and Coauthors, 2008b: Stratospheric impact of the Chisholm pyrocumulonimbus eruption: 2. Vertical profile perspective. *J. Geophys. Res.*, **113**, D08203, https://doi.org/10.1029/2007JD009147.

——, D. T. Lindsey, R. Servranckx, G. Yue, T. Trickl, R. Sica, P. Doucet, and S. Godin-Beekmann, 2010: The untold story of pyrocumulonimbus. *Bull. Amer. Meteor. Soc.*, **91**, 1193–1210, https://doi.org/10.1175/2010BAMS3004.1.

——, D. Peterson, and L. Di Girolamo, 2019: The primary convective pathway for observed wildfire emissions in the upper troposphere and lower stratosphere: A targeted reinterpretation. *J. Geophys. Res. Atmos.*, **124**, 13 254–13 272, https://doi.org/10.1029/2019JD031006.

——, G. P. Kablick, D. A. Peterson, R. A. Kahn, V. J. B. Flower, and C. J. Seftor, 2021: Quantifying the source term and uniqueness of the August 12, 2017 Pacific northwest PyroCb event. *J. Geophys. Res. Atmos.*, **126**, e2021JD034928, https://doi.org/10.1029/2021JD034928.

Gatebe, C. K., T. Varnai, R. Poudyal, C. Ichoku, and M. D. King, 2012: Taking the pulse of pyrocumulus clouds. *Atmos. Environ.*, **52**, 121–130, https://doi.org/10.1016/j.atmosenv.2012.01.045.

Giglio, L., J. Descloitres, C. O. Justice, and Y. J. Kaufman, 2003: An enhanced contextual fire detection algorithm for MODIS. *Remote Sens. Environ.*, **87**, 273–282, https://doi.org/10.1016/S0034-4257(03)00184-6.

——, W. Schroeder, and C. O. Justice, 2016: The collection 6 MODIS active fire detection algorithm and fire products. *Remote Sens. Environ.*, **178**, 31–41, https://doi.org/10.1016/j.rse.2016.02.054.

Haarig, M., A. Ansmann, H. Baars, C. Jimenez, I. Veselovskii, R. Engelmann, and D. Althausen, 2018: Depolarization and lidar ratios at 355, 532, and 1064 nm and microphysical properties of aged tropospheric and stratospheric Canadian wildfire smoke. *Atmos. Chem. Phys.*, **18**, 11 847–11 861, https://doi.org/10.5194/acp-18-11847-2018.

Hair, J. W., and Coauthors, 2008: Airborne High Spectral Resolution Lidar for profiling aerosol optical properties. *Appl. Opt.*, **47**, 6734–6752, https://doi.org/10.1364/AO.47.006734.

Hodshire, A. L., and Coauthors, 2021: Dilution impacts on smoke aging: Evidence in Biomass Burning Observation Project (BBOP) data. *Atmos. Chem. Phys.*, **21**, 6839–6855, https://doi.org/10.5194/acp-21-6839-2021.

Iguchi, T., T. Matsui, Z. Tao, D. Kim, C. M. Ichoku, L. Ellison, and J. Wang, 2018: NU-WRF aerosol transport simulation over West Africa: Effects of biomass burning on smoke aerosol distribution. *J. Appl. Meteor. Climatol.*, **57**, 1551–1573, https://doi.org/10.1175/JAMC-D-17-0278.1.

Jahn, L. G., M. J. Polen, L. G. Jahl, T. A. Brubaker, J. Somers, and R. C. Sullivan, 2020: Biomass combustion produces ice-active minerals in biomass-burning aerosol and bottom ash. *Proc. Natl. Acad. Sci. USA*, **117**, 21 928–21 937, https://doi.org/10.1073/pnas.1922128117.

Johnson, D., 2019: Incident Status Summary (ICS-209) for Williams Flats. Incident number WA-COA-190106, prepared 1700 PDT on 08-08-2019, 5 pp.

Jost, H.-J., and Coauthors, 2004: In-situ observations of mid-latitude forest fire plumes deep in the stratosphere. *Geophys. Res. Lett.*, **31**, L11101, https://doi.org/10.1029/2003GL019253.

Kablick, G. P., III, and Coauthors, 2018: The Great Slave Lake PyroCb of 5 August 2014: Observations, simulations, comparisons with regular convection, and impact on UTLS water vapor. *J. Geophys. Res. Atmos.*, **123**, 12 332–12 352, https://doi.org/10.1029/2018JD028965.

——, D. R. Allen, M. D. Fromm, and G. E. Nedoluha, 2020: Australian PyroCb smoke generates synoptic-scale stratospheric anticyclones. *Geophys. Res. Lett.*, **47**, e2020GL088101, https://doi.org/10.1029/2020GL088101.

Kahn, R. A., W. H. Li, C. Moroney, D. J. Diner, J. V. Martonchik, and E. Fishbein, 2007: Aerosol source plume physical characteristics from space-based multiangle imaging. *J. Geophys. Res.*, **112**, D11205, https://doi.org/10.1029/2006JD007647.

Kasischke, E. S., N. L. Christensen, and B. J. Stocks, 1995: Fire, global warming, and the carbon balance of boreal forests. *Ecol. Appl.*, **5**, 437–451, https://doi.org/10.2307/1942034.

Khaykin, S., and Coauthors, 2020: The 2019/20 Australian wildfires generated a persistent smoke-charged vortex rising up to 35 km altitude. *Commun. Earth Environ.*, **1**, 22, https://doi.org/10.1038/s43247-020-00022-5.

Kleinman, L. I., and Coauthors, 2020: Rapid evolution of aerosol particles and their optical properties downwind of wildfires in the western US. *Atmos. Chem. Phys.*, **20**, 13 319–13 341, https://doi.org/10.5194/acp-20-13319-2020.

Kochanski, A. K., D. V. Mallia, M. G. Fearon, J. Mandel, A. H. Souri, and T. Brown, 2019: Modeling wildfire smoke feedback mechanisms using a coupled fire-atmosphere model with a radiatively active aerosol scheme. *J. Geophys. Res. Atmos.*, **124**, 9099–9116, https://doi.org/10.1029/2019JD030558.

Kumar, S. S., D. P. Roy, L. Boschetti, and R. Kremens, 2011: Exploiting the power law distribution properties of satellite fire radiative power retrievals: A method to estimate fire radiative energy and biomass burned from sparse satellite observations. *J. Geophys. Res.*, **116**, D19303, https://doi.org/10.1029/2011JD015676.

Kumjian, M. R., 2013: Principles and applications of dual-polarization weather radar. Part I: Description of the polarimetric radar variables. *J. Oper. Meteor.*, **1**, 226–242, https://doi.org/10.15191/nwajom.2013.0119.

Laing, J. R., D. A. Jaffe, and J. R. Hee, 2016: Physical and optical properties of aged biomass burning aerosol from wildfires in Siberia and the western USA at the Mt. Bachelor Observatory. *Atmos. Chem. Phys.*, **16**, 15 185–15 197, https://doi.org/10.5194/acp-16-15185-2016.

Lang, T. J., S. A. Rutledge, B. Dolan, P. Krehbiel, W. Rison, and D. T. Lindsey, 2014: Lightning in wildfire smoke plumes observed in Colorado during summer 2012. *Mon. Wea. Rev.*, **142**, 489–507, https://doi.org/10.1175/MWR-D-13-00184.1.

Lareau, N. P., and C. B. Clements, 2016: Environmental controls on pyrocumulus and pyrocumulonimbus initiation and development. *Atmos. Chem. Phys.*, **16**, 4005–4022, https://doi.org/10.5194/acp-16-4005-2016.

——, and ——, 2017: The mean and turbulent properties of a wildfire convective plume. *J. Appl. Meteor. Climatol.*, **56**, 2289–2299, https://doi.org/10.1175/JAMC-D-16-0384.1.

LaRoche, K. T., and T. J. Lang, 2017: Observations of ash, ice, and lightning within pyrocumulus clouds using polarimetric NEXRAD radars and the National Lightning Detection Network. *Mon. Wea. Rev.*, **145**, 4899–4910, https://doi.org/10.1175/MWR-D-17-0253.1.

Lavoué, D., C. Liousse, H. Cachier, B. J. Stocks, and J. G. Goldammer, 2000: Modeling of carbonaceous particles emitted by boreal and temperate wildfires at northern latitudes. *J. Geophys. Res.*, **105**, 26 871–26 890, https://doi.org/10.1029/2000JD900180.

Leach, R. N., and C. V. Gibson, 2021: Assessing the potential for pyroconvection and wildfire blow ups. *J. Oper. Meteor.*, **9**, 47–61, https://doi.org/10.15191/nwajom.2021.0904.

Lestrelin, H., B. Legras, A. Podglajen, and M. Salihoglu, 2021: Smoke-charged vortices in the stratosphere generated by wildfires and their behaviour in both hemispheres: Comparing Australia 2020 to Canada 2017. *Atmos. Chem. Phys.*, **21**, 7113–7134, https://doi.org/10.5194/acp-21-7113-2021.

Livesey, N. J., M. D. Fromm, J. W. Waters, G. L. Manney, M. L. Santee, and W. G. Read, 2004: Enhancements in lower stratospheric CH3CN observed by the upper atmosphere research satellite microwave limb sounder following boreal forest fires. *J. Geophys. Res.*, **109**, D06308, https://doi.org/10.1029/2003JD004055.

McCarthy, N., H. McGowan, A. Guyot, and A. Dowdy, 2018: Mobile X-Pol radar: A new tool for investigating pyroconvection and associated wildfire meteorology. *Bull. Amer. Meteor. Soc.*, **99**, 1177–1195, https://doi.org/10.1175/BAMS-D-16-0118.1.

——, A. Guyot, A. Dowdy, and H. McGowan, 2019: Wildfire and weather radar: A review. *J. Geophys. Res. Atmos.*, **124**, 266–286, https://doi.org/10.1029/2018JD029285.

McNaughton, C. S., and Coauthors, 2007: Results from the DC-8 Inlet Characterization Experiment (DICE): Airborne versus surface sampling of mineral dust and sea salt aerosols. *Aerosol Sci. Technol.*, **41**, 136–159, https://doi.org/10.1080/02786820601118406.

McRae, R. H. D., J. J. Sharples, and M. Fromm, 2015: Linking local wildfire dynamics to pyroCb development. *Nat. Hazards Earth Syst. Sci.*, **15**, 417–428, https://doi.org/10.5194/nhess-15-417-2015.

Moore, R. H., and Coauthors, 2021: Sizing response of the Ultra-High Sensitivity Aerosol Spectrometer (UHSAS) and Laser Aerosol Spectrometer (LAS) to changes in submicron aerosol composition and refractive index. *Atmos. Meas. Tech.*, **14**, 4517–4542, https://doi.org/10.5194/amt-14-4517-2021.

Nimchuk, N., 1983: Wildfire behavior associated with upper ridge breakdown. Alberta Energy and Natural Resources Forest Service Rep. No. T/50, 45 pp.

Ottmar, R. D., D. V. Sandberg, C. L. Riccardi, and S. J. Prichard, 2007: An overview of the Fuel Characteristic Classification System – Quantifying, classifying, and creating fuelbeds for resource planning. *Can. J. For. Res.*, **37**, 2383–2393, https://doi.org/10.1139/X07-077.

Peterson, D. A., and J. Wang, 2013: A sub-pixel-based calculation of fire radiative power from MODIS observations: 2. Sensitivity analysis and potential fire weather application. *Remote Sens. Environ.*, **129**, 231–249, https://doi.org/10.1016/j.rse.2012.10.020.

——, ——, C. Ichoku, E. Hyer, and V. Ambrosia, 2013: A sub-pixel-based calculation of fire radiative power from MODIS observations: 1. Algorithm development and initial assessment. *Remote Sens. Environ.*, **129**, 262–279, https://doi.org/10.1016/j.rse.2012.10.036.

——, E. Hyer, and J. Wang, 2014: Quantifying the potential for high-altitude smoke injection in the North American boreal forest using the standard MODIS fire products and subpixel-based methods. *J. Geophys. Res. Atmos.*, **119**, 3401–3419, https://doi.org/10.1002/2013JD021067.

——, ——, J. R. Campbell, M. D. Fromm, J. W. Hair, C. F. Butler, and M. A. Fenn, 2015: The 2013 rim fire implications for predicting extreme fire spread, pyroconvection, and smoke emissions. *Bull. Amer. Meteor. Soc.*, **96**, 229–247, https://doi.org/10.1175/BAMS-D-14-00060.1.

——, ——, ——, J. E. Solbrig, and M. D. Fromm, 2017a: A conceptual model for development of intense pyrocumulonimbus in western North America. *Mon. Wea. Rev.*, **145**, 2235–2255, https://doi.org/10.1175/MWR-D-16-0232.1.

——, M. D. Fromm, J. E. Solbrig, E. J. Hyer, M. L. Surratt, and J. R. Campbell, 2017b: Detection and inventory of intense pyroconvection in western North America using GOES-15 daytime infrared data. *J. Appl. Meteor. Climatol.*, **56**, 471–493, https://doi.org/10.1175/JAMC-D-16-0226.1.

——, J. R. Campbell, E. J. Hyer, M. D. Fromm, G. P. Kablick, J. H. Cossuth, and M. T. DeLand, 2018: Wildfire-driven thunderstorms cause a volcano-like stratospheric injection of smoke. *npj Climate Atmos. Sci.*, **1**, 30, https://doi.org/10.1038/s41612-018-0039-3.

——, and Coauthors, 2021: Australia's Black Summer pyrocumulonimbus super outbreak reveals potential for increasingly extreme stratospheric smoke events. *npj Climate Atmos. Sci.*, **4**, 38, https://doi.org/10.1038/s41612-021-00192-9.

Polivka, T. N., J. Wang, L. T. Ellison, E. J. Hyer, and C. M. Ichoku, 2016: Improving nocturnal fire detection with the VIIRS day–night band. *IEEE Trans. Geosci. Remote Sens.*, **54**, 5503–5519, https://doi.org/10.1109/TGRS.2016.2566665.

Portin, H., and Coauthors, 2012: Biomass burning aerosols observed in eastern Finland during the Russian wildfires in summer 2010 – Part 1: In-situ aerosol characterization. *Atmos. Environ.*, **47**, 269–278, https://doi.org/10.1016/j.atmosenv.2011.10.067.

Potter, B. E., 2005: The role of released moisture in the atmospheric dynamics associated with wildland fires. *Int. J. Wildland Fire*, **14**, 77–84, https://doi.org/10.1071/WF04045.

——, 2012: Atmospheric interactions with wildland fire behaviour – I. Basic surface interactions, vertical profiles and synoptic structures. *Int. J. Wildland Fire*, **21**, 779–801, https://doi.org/10.1071/WF11128.

Prichard, S. J., A. G. Andreu, R. D. Ottmar, and E. Eberhardt, 2019: Fuel Characteristic Classification System (FCCS) field sampling and fuelbed development guide. General Tech. Rep. PNW-GTR-972, U.S. Department of Agriculture, 77 pp., https://doi.org/10.2737/PNW-GTR-972.

Ray, E. A., and Coauthors, 2004: Evidence of the effect of summertime midlatitude convection on the subtropical lower stratosphere from CRYSTAL-FACE tracer measurements. *J. Geophys. Res.*, **109**, D18304, https://doi.org/10.1029/2004JD004655.

Reid, J. S., R. Koppmann, T. F. Eck, and D. P. Eleuterio, 2005a: A review of biomass burning emissions Part II: Intensive physical properties of biomass burning particles. *Atmos. Chem. Phys.*, **5**, 799–825, https://doi.org/10.5194/acp-5-799-2005.

——, and Coauthors, 2005b: A review of biomass burning emissions Part III: Intensive optical properties of biomass burning particles. *Atmos. Chem. Phys.*, **5**, 827–849, https://doi.org/10.5194/acp-5-827-2005.

——, and Coauthors, 2017: Ground-based high spectral resolution lidar observation of aerosol vertical distribution in the summertime southeast United States. *J. Geophys. Res. Atmos.*, **122**, 2970–3004, https://doi.org/10.1002/2016JD025798.

Reutter, P., and Coauthors, 2014: 3-D model simulations of dynamical and microphysical interactions in pyroconvective clouds under idealized conditions. *Atmos. Chem. Phys.*, **14**, 7573–7583, https://doi.org/10.5194/acp-14-7573-2014.

Rodriguez, B., N. P. Lareau, D. E. Kingsmill, and C. B. Clements, 2020: Extreme pyroconvective updrafts during a megafire. *Geophys. Res. Lett.*, **47**, e2020GL089001, https://doi.org/10.1029/2020gl089001.

Rosenfeld, D., and G. Gutman, 1994: Retrieving microphysical properties near the tops of potential rain clouds by multispectral analysis of AVHRR data. *Atmos. Res.*, **34**, 259–283, https://doi.org/10.1016/0169-8095(94)90096-5.

——, M. Fromm, J. Trentmann, G. Luderer, M. O. Andreae, and R. Servranckx, 2007: The Chisholm firestorm: Observed microstructure, precipitation and lightning activity of a pyro-cumulonimbus. *Atmos. Chem. Phys.*, **7**, 645–659, https://doi.org/10.5194/acp-7-645-2007.

——, U. Lohmann, G. B. Raga, C. D. O'Dowd, M. Kulmala, S. Fuzzi, A. Reissell, and M. O. Andreae, 2008: Flood or drought: How do aerosols affect precipitation? *Science*, **321**, 1309–1313, https://doi.org/10.1126/science.1160606.

——, and Coauthors, 2014: Global observations of aerosol-cloud-precipitation-climate interactions. *Rev. Geophys.*, **52**, 750–808, https://doi.org/10.1002/2013RG000441.

Saide, P. E., and Coauthors, 2015: Revealing important nocturnal and day-to-day variations in fire smoke emissions through a multiplatform inversion. *Geophys. Res. Lett.*, **42**, 3609–3618, https://doi.org/10.1002/2015GL063737.

Schroeder, W., I. Csiszar, L. Giglio, and C. C. Schmidt, 2010: On the use of fire radiative power, area, and temperature estimates to characterize biomass burning via moderate to coarse spatial resolution remote sensing data in the Brazilian Amazon. *J. Geophys. Res.*, **115**, D21121, https://doi.org/10.1029/2009JD013769.

——, and Coauthors, 2014: Integrated active fire retrievals and biomass burning emissions using complementary near-coincident ground, airborne and spaceborne sensor data. *Remote Sens. Environ.*, **140**, 719–730, https://doi.org/10.1016/j.rse.2013.10.010.

Soja, A. J., W. R. Cofer, H. H. Shugart, A. I. Sukhinin, P. W. Stackhouse, D. J. McRae, and S. G. Conard, 2004: Estimating fire emissions and disparities in boreal Siberia (1998–2002). *J. Geophys. Res.*, **109**, D14S06, https://doi.org/10.1029/2004JD004570.

Spanu, A., M. Dollner, J. Gasteiger, T. P. Bui, and B. Weinzierl, 2020: Flow-induced errors in airborne in situ measurements of aerosols and clouds. *Atmos. Meas. Tech.*, **13**, 1963–1987, https://doi.org/10.5194/amt-13-1963-2020.

Sullivan, A. L., and S. Matthews, 2013: Determining landscape fine fuel moisture content of the Kilmore East 'Black Saturday' wildfire using spatially-extended point-based models. *Environ. Modell. Software*, **40**, 98–108, https://doi.org/10.1016/j.envsoft.2012.08.008.

Torres, O., and Coauthors, 2020: Stratospheric injection of massive smoke plume from Canadian boreal fires in 2017 as seen by DSCOVR-EPIC, CALIOP, and OMPS-LP observations. *J. Geophys. Res. Atmos.*, **125**, e2020JD032579, https://doi.org/10.1029/2020JD032579.

Tory, K. J., and J. D. Kepert, 2021: Pyrocumulonimbus firepower threshold: Assessing the atmospheric potential for pyroCb. *Wea. Forecasting*, **36**, 439–456, https://doi.org/10.1175/WAF-D-20-0027.1.

——, W. Thurston, and J. D. Kepert, 2018: Thermodynamics of pyrocumulus: A conceptual study. *Mon. Wea. Rev.*, **146**, 2579–2598, https://doi.org/10.1175/MWR-D-17-0377.1.

Waibel, A. E., H. Fischer, F. G. Wienhold, P. C. Siegmund, B. Lee, J. Ström, J. Lelieveld, and P. J. Crutzena, 1999: Highly elevated carbon monoxide concentrations in the upper troposphere and lowermost stratosphere at northern midlatitudes during the STREAM II summer campaign in 1994. *Chemosphere*, **1**, 233–248, https://doi.org/10.1016/S1465-9972(99)00027-6.

Wang, J., and Coauthors, 2020: Detecting nighttime fire combustion phase by hybrid application of visible and infrared radiation from Suomi NPP VIIRS. *Remote Sens. Environ.*, **237**, 111466, https://doi.org/10.1016/j.rse.2019.111466.

Westphal, D. L., and O. B. Toon, 1991: Simulations of microphysical, radiative, and dynamic processes in a continental-scale forest-fire smoke plume. *J. Geophys. Res.*, **96**, 22 379–22 400, https://doi.org/10.1029/91JD01956.

Wooster, M. J., B. Zhukov, and D. Oertel, 2003: Fire radiative energy for quantitative study of biomass burning: Derivation from the BIRD experimental satellite and comparison to MODIS fire products. *Remote Sens. Environ.*, **86**, 83–107, https://doi.org/10.1016/S0034-4257(03)00070-1.

——, G. Roberts, G. L. W. Perry, and Y. J. Kaufman, 2005: Retrieval of biomass combustion rates and totals from fire radiative power observations: FRP derivation and calibration relationships between biomass consumption and fire radiative energy release. *J. Geophys. Res.*, **110**, D24311, https://doi.org/10.1029/2005JD006318.

Yu, P., and Coauthors, 2016: Surface dimming by the 2013 Rim Fire simulated by a sectional aerosol model. *J. Geophys. Res. Atmos.*, **121**, 7079–7087, https://doi.org/10.1002/2015JD024702.

——, and Coauthors, 2019: Black carbon lofts wildfire smoke high into the stratosphere to form a persistent plume. *Science*, **365**, 587–590, https://doi.org/10.1126/science.aax1748.

——, and Coauthors, 2021: Persistent stratospheric warming due to 2019–2020 Australian wildfire smoke. *Geophys. Res. Lett.*, **48**, e2021GL092609, https://doi.org/10.1029/2021GL092609.

Zhang, Y. W., J. W. Fan, T. Logan, Z. Q. Li, and C. R. Homeyer, 2019: Wildfire impact on environmental thermodynamics and severe convective storms. *Geophys. Res. Lett.*, **46**, 10 082–10 093, https://doi.org/10.1029/2019GL084534.

Ziemba, L. D., and Coauthors, 2013: Airborne observations of aerosol extinction by in situ and remote-sensing techniques: Evaluation of particle hygroscopicity. *Geophys. Res. Lett.*, **40**, 417–422, https://doi.org/10.1029/2012GL054428.